



# Effects of Initial Conditions on Magnetic Reconnection in a Solar Transient

Satyam Agarwal<sup>1,2</sup> · Ramit Bhattacharyya<sup>1</sup> · Thomas Wiegelmann<sup>3</sup>

Received: 29 December 2021 / Accepted: 1 June 2022 / Published online: 18 July 2022  
© The Author(s), under exclusive licence to Springer Nature B.V. 2022

## Abstract

Coronal magnetic field extrapolations are necessary to understand the magnetic field morphology of the source region in solar coronal transients. The extrapolation models are broadly classified into nonforce-free and force-free, depending on whether the model allows for a Lorentz force or not. Presently, these models are employed to carry out state-of-the-art data-driven and data-constrained magnetohydrodynamics (MHD) simulations to explore magnetic reconnection (MR)—the underlying cause of the transients. It is then imperative to study the influence of different extrapolation models on simulated evolution. For this purpose, the numerical model EULAG-MHD is employed to carry out simulations with different initial magnetic and velocity fields obtained through nonforce-free and force-free extrapolations. The selected active region is NOAA 11977, hosting a C6.6 class eruptive flare. Both extrapolations are found to be in good agreement with the observed line-of-sight and transverse magnetic fields. Further, a morphological comparison on the global scale and particularly for selected topologies, such as a magnetic null point and a hyperbolic flux tube (HFT), suggests that similar magnetic field line structures are reproducible in both models, although the extent of agreement between the two varies. Astoundingly, generation of a three-dimensional null near the HFT is observed in all the simulations, inferring the evolution to be independent of the particular initial field configuration. Moreover, the magnetic field lines (MFLs) undergoing MRs at the null point and HFT evolve similarly, further confirming the near independence of reconnection details on the chosen initial conditions. Consequently, both the extrapolation techniques can be suitable for initiating data-driven and data-constrained simulations.

**Keywords** Flare · Extrapolation · Simulation · Dynamics

---

✉ S. Agarwal  
[satyam@prl.res.in](mailto:satyam@prl.res.in)

R. Bhattacharyya  
[ramit@prl.res.in](mailto:ramit@prl.res.in)

T. Wiegelmann  
[wiegelmann@mps.mpg.de](mailto:wiegelmann@mps.mpg.de)

<sup>1</sup> Udaipur Solar Observatory, Physical Research Laboratory, Udaipur 313 001, India

<sup>2</sup> Indian Institute of Technology Gandhinagar, Palaj, Gujarat, India

<sup>3</sup> Max-Planck-Institut für Sonnensystemforschung, Justus-von-Liebig-Weg 3, 37077 Göttingen, Germany

## 1. Introduction

Solar transients such as flares, coronal mass ejections (CMEs) and jets are sudden episodic energy releases and plasma outbursts. The transients are important both as a fundamental phenomena and because of their influence on the near-Earth space weather. It is then imperative to understand their source-region dynamics. Magnetic reconnection is generally believed to be one of the underlying mechanisms of the transients (Shibata and Magara, 2011). Several details such as the triggering mechanism, reconnection rate, energetics, and multiscale behaviors are central to a comprehensive understanding of magnetic reconnection and, hence, the transients. The MRs occur at local diffusive scales of MHD leading to breakage and reconfiguration of MFLs, while the released energy is stored in its magnetic form on the global scales, where the MFLs are tied to the plasma parcels because of the flux freezing (Zweibel and Yamada, 2016). The two scales are not independent, but feed each other, as envisaged in the numerical simulation of Kumar et al. (2016). The MRs are dissipative processes, converting magnetic energy into heat, which is lost irrecoverably from the system. Consequently, a parallel can be drawn with the dissipative dynamics of a system governed by classical mechanics. Conceptually, the analogy infers the global evolution of MFLs to be relatively insensitive to the initial condition as, presumably, dissipation erases the memory of a system. The inference can have rather strong implications in the data-driven or data-constrained numerical simulation of transients where the initial coronal magnetic field is extrapolated from photospheric magnetograms. In particular, it raises the expectation that two simulations having analogous initial MFL morphologies can yield similar MRs—a problem imperatively interesting and novel to explore. Toward such exploration, here, we consider the two most widely used approaches for extrapolation: the nonlinear force-free field (NLFFF) and the nonforce-free field (NFFF)—their nomenclature being based on whether the exerted Lorentz force is zero or not.

The overall work flow selects an active region undergoing a flare, extrapolates the magnetic field using the two approaches and uses them as input for the MHD simulations. The simulation results are then compared to draw conclusions. To our understanding, the proof-of-concept numerical experiment reported in this paper is the first of its kind and merits attention.

As background, the analytical expression of NLFFF treats both the coronal plasma and the photosphere to be exactly force free. However, its computational implementation allows for a residual Lorentz force because of the unavoidable numerical errors. Following Inoue, Hayashi, and Kusano (2016), this residual force is used as a perturbation to initiate one of the NLFFF simulations described in the paper. The expectation is an appreciable change in kinetic energy if the NLFFF solution belongs to one of its unstable branches. Unstable branches of NLFFF are well studied in the literature. For instance, the Titov–Démoulin equilibrium (Titov and Démoulin, 1999) becomes unstable when the radius of curvature of the flux tube is comparable in value with the size of the active region. Additionally, force-free flux ropes are found to become either torus or kink unstable, when the decay index  $n \approx 1.5$  (Kliem and Török, 2006) or the normalized axial wave number  $k' > 1$  (Kliem et al., 2010). The corresponding rise of the flux tube can provide a scenario for eruptive flares, which is different from the one assisted by reconnections. Contrarily, the Lorentz force at the photosphere is nonzero for the NFFF but generally decays sharply with height and is  $\in [5.8\%, 0.04\%]$  of its photospheric value for height  $\in [3.2, 98.6]$  Mm, making it approximately force-free at the corona for the AR under consideration. We rely on these properties, elaborated later, of the extrapolation models to carry out the simulations described in the paper. Notably, the MHD model used for comparison is idealized—for instance, the flow

is incompressible and focuses only on the dynamics of MFLs along with locations of magnetic reconnections but does not elucidate on the emissions, preflare activities, and other complexities observed in an actual flare.

For the NLFFF, we choose the extrapolation model based on the principle of weighted optimization method (Wiegelmann, 2004, Wiegelmann, Inhester, and Sakurai, 2006, Wiegelmann and Inhester, 2010) because of its wide acceptance in contemporary research. It typically models the force-free region of the solar atmosphere between the upper photosphere and the lower corona where  $\beta \ll 1$  (Gary, 2001). Such a choice seems appropriate because NLFFF can account for the free magnetic energy released in the form of electromagnetic radiations and energetic particles during eruptive events (Wiegelmann and Sakurai, 2021). Further, previous works on modeling of solar-active regions have shown the capability of this NLFFF scheme to adequately reproduce coronal loops (Warren et al., 2018), magnetic flux rope structures (Mitra et al., 2020), and complex magnetic topologies like magnetic null points and quasiseparatrix layers (Zhao et al., 2014, Joshi, Joshi, and Mitra, 2021). The second initial condition employs the NFFF extrapolation based on the Minimum Dissipation Rate principle (MDR: Bhattacharyya and Janaki, 2004, Bhattacharyya et al., 2007, Hu and Dasgupta, 2008). NFFF gains its importance from an implicit presence of a nonzero Lorentz force that can drive the plasma dynamics. Earlier works have confirmed its efficacy in exploring several scenarios of observational interest. Examples include MFL evolution leading to solar flares and blowout jets (Prasad et al., 2018, Nayak et al., 2019, Nayak, Bhattacharyya, and Kumar, 2021) along with the development of current sheets around null points (Kumar and Bhattacharyya, 2016) and quasiseparatrix layers (Kumar et al., 2021).

The photospheric magnetogram at 02:48 UT of AR 11977 on 17th February, 2014 is selected as the marker to determine the extent of correlation between the observed and the modeled magnetic fields on the bottom boundary. The selection is motivated by the occurrence of a C6.6 class flare that peaked at 03:04 UT. In general, MHD simulations with NLFFF extrapolation (e.g., Jiang et al., 2013, Kliem et al., 2013, Amari, Canou, and Aly, 2014, Inoue et al., 2014, 2015) and NFFF extrapolation (Prasad et al., 2018, Nayak et al., 2019, Nayak, Bhattacharyya, and Kumar, 2021) have been successful in explaining the coronal dynamics leading to eruptive events. In the same spirit, active region NOAA 11977 has been simulated here to understand the details of its evolution and the role played by models in this context. The results show the simulated dynamics to be nearly independent of the particular initial state and importantly, spontaneous generations of a three-dimensional null in all the cases.

The paper is organized as follows. Section 2 discusses the active region and the C6.6 class flare. It also describes the observations relevant to interpret the simulations. In Section 3, we present the quantitative and topological differences between the nonlinear force-free and nonforce-free extrapolated fields. The numerical MHD model is discussed in Section 4. The results are presented in Section 5, while Section 6 summarizes the important findings.

## 2. Active Region and Flare Event

The C6.6 class eruptive flare on 2014 February 17 from active region NOAA 11977 with heliographic coordinates S13W05 is selected since (a) its location is approximately disk centered, so that the error in the observed photospheric magnetic field is small and (b) the photospheric magnetic flux integrated over the active region, changes minimally during the course of the flare and a line-tied boundary condition can be used to simplify the simulations. Figure 1(a) shows the Geostationary Operational Environmental Satellite (GOES) soft X-ray

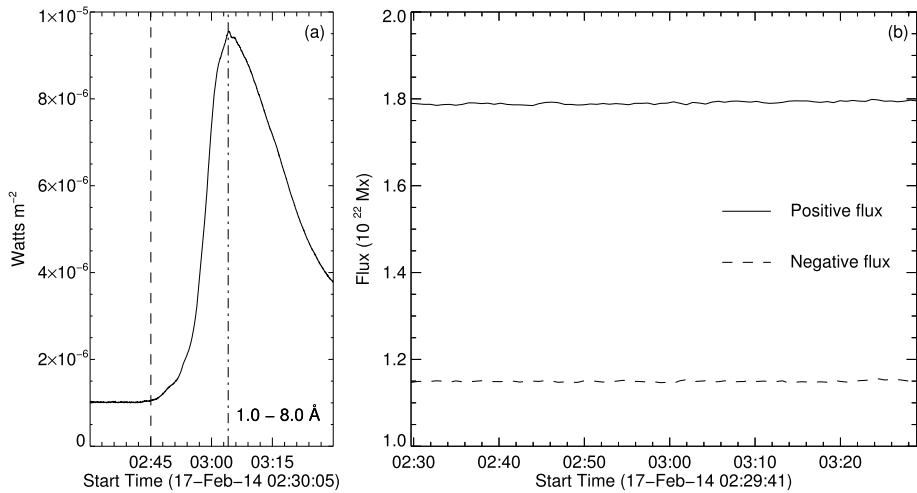


**Figure 1** (a) GOES soft X-ray flux for a one-hour period starting at 02:30 UT in the 1–8 Å channel. The *dashed black line* marks the rising phase at  $\sim 02:45$  UT and the *dashed-dot line* marks the peak time of the flare. (b) Photospheric flux during a one-hour period starting from 02:30 UT, where the *solid line* denotes positive flux and the *dashed line* denotes negative flux.

flux during the course of the flare in the 1–8 Å channel, revealing a gradual rise in intensity around  $\sim 02:45$  UT, peaking at 03:04 UT. Importantly, Figure 1(b) shows the evolution of the horizontally averaged positive (*solid*) and negative (*dashed*) photospheric magnetic flux obtained from *hmi.M\_45* series of Helioseismic Magnetic Imager (SDO/HMI; Schou et al., 2012, Scherrer et al., 2012) for a duration of  $\sim 1$  h, starting around 02:30 UT. The magnetic flux is reasonably constant during the flare, the relative changes for both positive and negative fluxes being well within 1%.

Figure 2 illustrates the temporal evolution of the flaring event in EUV (131 Å) channel of Atmospheric Imaging Assembly (AIA; Lemen et al., 2012) onboard Solar Dynamics Observatory (SDO; Pesnell, Thompson, and Chamberlin, 2012) for a duration of  $\sim 35$  m, starting around 02:45 UT. Panels (b), (c), and (f) mark the approximate spatial locations of brightenings ( $b_1$ ,  $b_2$ ,  $b_3$ , and  $b_4$ ) identified at different instances during the flare. Importantly, we recognize a *lasso* structure, visible in Panel (e), which prominently displays the overall geometry of the flaring region.

### 3. The Extrapolated Magnetic Field: NFFF and NLFFF

The coronal field is extrapolated at 02:48:00 UT, using the *hmi.sharp\_cea\_720s* (Bobra et al., 2014) data series from SDO/HMI, where CEA refers to the Cylindrical Equal Area (Calabretta and Greisen, 2002) projection. The data provides radial ( $B_r$ ), toroidal ( $B_t$ ), and poloidal ( $B_p$ ) components of magnetic field, which satisfy the following relations in a Cartesian coordinate system (a)  $B_z = B_r$ , (b)  $B_x = B_p$ , and (c)  $B_y = -B_t$ . The dimension of the SHARP series corresponding to HARP number 3740 for active region NOAA 11977 is  $906 \times 540$  pixels.

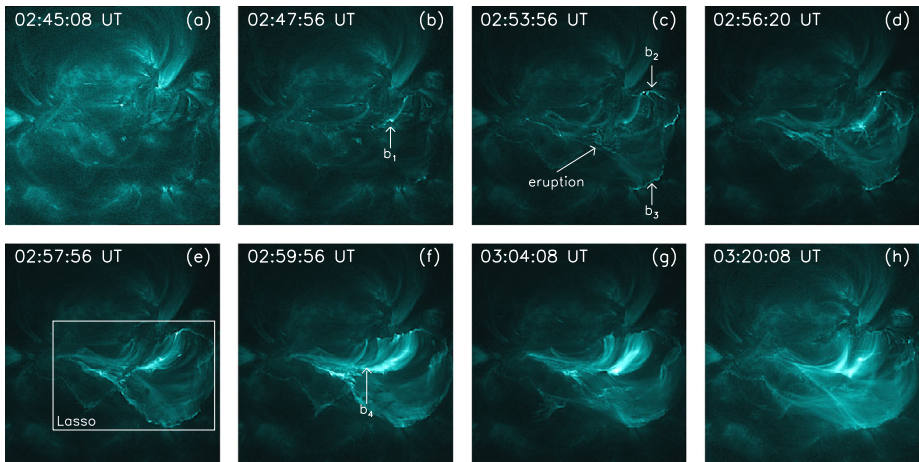


**Figure 2** Snapshots from the temporal evolution of active region NOAA 11977 in the Extreme Ultraviolet (131 Å) channel of SDO/AIA, starting around 02:45 UT. Panels (b), (c), and (f) mark the brightenings  $b_1$ ,  $b_2$ ,  $b_3$ , and  $b_4$  identified during the course of the flare. Panel (e) highlights the *lasso* structure that describes the overall flaring configuration. Panel (g) and Panel (h) correspond to the peak time and termination time of the flare, respectively.

### 3.1. NLFFF Extrapolation

The NLFFF equations are given by

$$(\nabla \times \mathbf{B}) \times \mathbf{B} = \mathbf{0}, \tag{1}$$

$$\nabla \cdot \mathbf{B} = 0, \tag{2}$$

which have to be solved together with the photospheric boundary condition

$$\mathbf{B} = \mathbf{B}_{\text{obs}} \text{ on the bottom boundary.} \tag{3}$$

$\mathbf{B}$  is the 3D magnetic field and  $\mathbf{B}_{\text{obs}}$  the magnetic field vector deduced from measurements in the photosphere. As an initial test, one has to check if the observed vector magnetogram is consistent with the assumption of a force-free field, which can be done by computing a number of dimensionless quantities, which have been introduced in Wiegelmann, Inhester, and Sakurai (2006), namely the flux balance  $\epsilon_{\text{flux}}$ , the net force balance  $\epsilon_{\text{force}}$ , and the net torque balance  $\epsilon_{\text{torque}}$ :

$$\epsilon_{\text{flux}} = \frac{\int_S B_z}{\int_S |B_z|},$$

$$\epsilon_{\text{force}} = \frac{|\int_S B_x B_z| + |\int_S B_y B_z| + |\int_S (B_x^2 + B_y^2) - B_z^2|}{\int_S (B_x^2 + B_y^2 + B_z^2)},$$

$$\epsilon_{\text{torque}} = \frac{|\int_S x((B_x^2 + B_y^2) - B_z^2)| + |\int_S y((B_x^2 + B_y^2) - B_z^2)| + |\int_S y B_x B_z - x B_y B_z|}{\int_S \sqrt{x^2 + y^2} (B_x^2 + B_y^2 + B_z^2)}.$$

For ideal force-free consistent boundary conditions, these criteria should be zero. For  $\epsilon_{\text{flux}}$ , the field of view has to be chosen accordingly. For measured magnetograms, the dimension-

**Table 1** Summary of the parameters used in the NLFFF extrapolation.

$\mu_1$	$\mu_2$	$\mu_3$	$\mu_4$	$w_f$	$w_d$	$\nu$	$w_{\text{los}}$	$w_{\text{trans}}$
1	1	0.01	0.01	1	1	0.001	1	$B_T/\text{max}(B_T)$

less quantities are not zero, but have finite values. If the quantities are low (below about 0.1), the boundary conditions are considered sufficiently force-free consistent and can be used as boundary condition  $\mathbf{B}_{\text{obs}}$  in Equation 3, as was done for HMI-data in Wiegelmann et al. (2012). Unfortunately, many photospheric vector-field measurements are not force-free consistent in the sense that  $\epsilon_{\text{force}}$  and  $\epsilon_{\text{torque}}$  are larger than about 0.1. For the data set used in this work, the corresponding values are  $\epsilon_{\text{flux}} \sim 0.2326$ ,  $\epsilon_{\text{force}} \sim 0.1590$ , and  $\epsilon_{\text{torque}} \sim 0.1690$ . Finite forces and torque in the photosphere are naturally caused by the finite plasma beta. The Lorentz force does not vanish in the photosphere for these cases and is compensated by other plasma forces. In these cases, the photospheric measurements cannot be used directly as boundary condition in Equation 3 and a preprocessing procedure, as introduced in Wiegelmann, Inhester, and Sakurai (2006) has to be applied to derive force-free consistent boundary conditions  $\mathbf{B}_{\text{obs}}$ . We summarize the preprocessing procedure briefly. A 2D-functional

$$L_p = \mu_1 L_1 + \mu_2 L_2 + \mu_3 L_3 + \mu_4 L_4 \tag{4}$$

is defined, which has the individual terms  $L_{i=1,4}$  as

$$L_1 = \left[ \left( \sum_p B_x B_z \right)^2 + \left( \sum_p B_y B_z \right)^2 + \left( \sum_p B_z^2 - B_x^2 - B_y^2 \right)^2 \right], \tag{5}$$

$$L_2 = \left[ \left( \sum_p x (B_z^2 - B_x^2 - B_y^2) \right)^2 + \left( \sum_p y (B_z^2 - B_x^2 - B_y^2) \right)^2 + \left( \sum_p (y B_x B_z - x B_y B_z) \right)^2 \right], \tag{6}$$

$$L_3 = \left[ \sum_p (B_x - B_x^{\text{obs}})^2 + \sum_p (B_y - B_y^{\text{obs}})^2 + \sum_p (B_z - B_z^{\text{obs}})^2 \right], \tag{7}$$

$$L_4 = \left[ \sum_p ((\Delta B_x)^2 + (\Delta B_y)^2 + (\Delta B_z)^2) \right], \tag{8}$$

and  $\mu_i$  are weighting factors for the corresponding terms, as specified in Table 1. The first and second terms represent the force balance and torque balance conditions (see Aly, 1989 for details). The third term corresponds to the difference between the preprocessed and measured values in the photosphere, while the last term controls smoothing. The output of the minimized 2D functional  $L_p$  provides a force-free consistent magnetogram and for convenience we call this output of the preprocessing again  $\mathbf{B}_{\text{obs}}$ . For the dataset used in this work, after preprocessing,  $\epsilon_{\text{flux}} \sim 0.2466$ ,  $\epsilon_{\text{force}} \sim 0.0005$ , and  $\epsilon_{\text{torque}} \sim 0.0015$ . This preprocessed magnetogram is used as a boundary condition for the 3D NLFFF-modelling. To do so, we solve Equations 1–3 with the help of an optimization principle. The method was originally proposed in Wheatland, Sturrock, and Roumeliotis (2000) and further developed

in Wiegelmann (2004) and Wiegelmann and Inhester (2010). Intensive tests of the methods with application to active-region vector magnetograms from HMI have been done in Wiegelmann et al. (2012). The optimization principle minimizes a functional defined as

$$L = \int_V w_f \frac{|(\nabla \times \mathbf{B}) \times \mathbf{B}|^2}{B^2} d^3x + \int_V w_d |\nabla \cdot \mathbf{B}|^2 d^3x + \nu \int_S (\mathbf{B} - \mathbf{B}^{\text{obs}}) \cdot \mathbf{W} \cdot (\mathbf{B} - \mathbf{B}^{\text{obs}}) dS, \tag{9}$$

where  $w_f$  and  $w_d$  are weighting functions toward the lateral and top boundaries of the computational box (see Wiegelmann, 2004 for details). The first and second terms correspond to the Lorentz force and divergence of the 3D magnetic field. The third term is evaluated only over the bottom boundary, whereas here  $\mathbf{B}^{\text{obs}}$  is the magnetic field vector in the bottom boundary after preprocessing.  $\mathbf{W}$  is a diagonal matrix whose elements ( $w_{\text{los}}$ ,  $w_{\text{trans}}$ , and  $w_{\text{trans}}$ ) are inversely proportional to the local measurement error and  $\nu$  is the Lagrange multiplier. With this definition, the bottom boundary is allowed to relax during the iterative procedure (see Wiegelmann et al. 2012 for details). The values of the parameters are listed in Table 1.

We compute the NLFFF extrapolations with a bottom boundary grid of  $896 \times 528$  pixels and the vertical extent is 272 pixels. In physical lengths the size is  $\sim 324.8 \text{ Mm} \times 191.4 \text{ Mm} \times 98.6 \text{ Mm}$ .

### 3.2. NFFF Extrapolation

A rationale for NFFF extrapolation can be found in the appendix of Mitra et al. (2018). Here, we reiterate its salient features for completeness. A dimensional analysis leads to the following approximation for the ratio of the Lorentz force to the rate of change of momentum

$$\frac{|\mathbf{J} \times \mathbf{B}|}{\left| \rho \frac{dv}{dt} \right|} \sim \frac{\mathbf{B}^2}{L} \frac{t}{\rho v} \sim \frac{\mathbf{B}^2}{\rho v^2} \sim \frac{\mathbf{B}^2}{\rho v_{\text{th}}^2} \frac{v_{\text{th}}^2}{v^2} \sim \frac{1}{\beta} \frac{v_{\text{th}}^2}{v^2}, \tag{10}$$

with  $v_{\text{th}}$  and  $\mathbf{J} = \nabla \times \mathbf{B}$  being the thermal velocity and the volume current density. The above expression can be further simplified to

$$\frac{|\mathbf{J} \times \mathbf{B}|}{\left| \rho \frac{dv}{dt} \right|} \sim \frac{1}{\beta}, \tag{11}$$

by recognizing the photospheric flow  $\sim 1 \text{ km s}^{-1}$  (Vekstein, 2016; Khlystova and Toriumi, 2017), while the thermal speed turns out to be  $\sim 1 \text{ km s}^{-1}$ . The ratio of thermal to magnetic pressure is denoted by  $\beta$ , which is  $\approx 1$  on the photosphere. Equation 11 then yields

$$|\mathbf{J} \times \mathbf{B}| \sim \left| \rho \frac{dv}{dt} \right|, \tag{12}$$

making it a plausible driver for photospheric motions and an apt candidate to initiate MHD simulations. The NFFF extrapolation exploits a magnetic field  $\mathbf{B}$  satisfying an inhomogeneous double-curl Beltrami equation (Bhattacharyya et al., 2007)

$$\nabla \times (\nabla \times \mathbf{B}) + a \nabla \times \mathbf{B} + b \mathbf{B} = \nabla \psi, \tag{13}$$

having  $a$  and  $b$  as constants. The solenoidality of  $\mathbf{B}$  imposes  $\nabla^2\psi = 0$ . Notably, the double-curl equation represents a self-organized state satisfying the MDR principle, (see Bhat-tacharyya and Janaki, 2004, and references therein for details).

Toward solving the double-curl equation, an auxiliary field  $\mathbf{B}' = \mathbf{B} - (\nabla\psi)/b$  (Hu and Dasgupta, 2008) satisfying the corresponding homogeneous equation is constructed. The equation represents a two-fluid steady state (Mahajan and Yoshida, 1998) and has a solution

$$\mathbf{B}' = \sum_{i=1,2} \mathbf{B}_i. \tag{14}$$

The  $\mathbf{B}_i$  are Chandrasekhar–Kendall eigenfunctions (Chandrasekhar and Kendall, 1957), obeying force-free equations

$$\nabla \times \mathbf{B}_i = \alpha_i \mathbf{B}_i, \tag{15}$$

with constant twists  $\alpha_i$ , and form a complete orthonormal set when the eigenvalues are real (Yoshida and Giga, 1990). Straightforwardly,

$$\mathbf{B} = \sum_{i=1,2} \mathbf{B}_i + \mathbf{B}_3, \tag{16}$$

where  $\mathbf{B}_3 = (\nabla\psi)/b$  is a potential field. Combining Equations (15) and (16),

$$\begin{pmatrix} \mathbf{B}_1 \\ \mathbf{B}_2 \\ \mathbf{B}_3 \end{pmatrix} = \mathcal{V}^{-1} \begin{pmatrix} \mathbf{B} \\ \nabla \times \mathbf{B} \\ \nabla \times (\nabla \times \mathbf{B}) \end{pmatrix}, \tag{17}$$

where the matrix  $\mathcal{V}$  is a Vandermonde matrix having elements  $\alpha_j^{i-1}$  for  $i, j = 1, 2, 3$ , and  $\alpha_3 = 0$  (Hu and Dasgupta, 2008).

The double-curl equation being of second order, ideally, two layers of magnetogram data are required to attempt an extrapolation. However, a workable solution can be achieved by following the technique documented in Hu and Dasgupta (2008). The technique, in brief, selects a pair of  $\alpha_i$  and set  $\mathbf{B}_3 = 0$ . The pair is used to calculate the  $z$ -components of  $\mathbf{B}_1$  and  $\mathbf{B}_2$  at the bottom boundary, using the  $B_z$  from the magnetogram. Employing a linear force-free solver and using  $B_{1z}, B_{2z}$  along with the pair of  $\alpha_i$ , the transverse components of  $\mathbf{B}_1$  and  $\mathbf{B}_2$  are extrapolated. Subsequently, an optimal pair of  $\alpha_i$  is obtained by minimizing the average normalized deviation of the magnetogram transverse field ( $\mathbf{B}_t$ ) from its extrapolated value ( $\mathbf{b}_t = \mathbf{B}_{1t} + \mathbf{B}_{2t}$ ), quantified as

$$E_n = \sum_{i=1}^M |\mathbf{B}_{t,i} - \mathbf{b}_{t,i}| / \sum_{i=1}^M |\mathbf{B}_{t,i}|, \tag{18}$$

where  $M = N^2$  is the total number of grid points on the transverse plane. The  $E_n$  is further reduced by using  $\mathbf{B}_3 = (\nabla\psi)/b$  as a corrector component field for the given pair of  $\alpha$ . The procedure is repeated until the value of  $E_n$  approximately saturates with the number of iterations, making the solution unique. Importantly, the procedure alters the bottom boundary and a correlation with the original magnetogram is necessary to check for the accuracy.

A unique advantage in the NFFF extrapolation is the absence of any upper bound of the field-line twist, quantified by the field-aligned current

$$\tau \equiv \frac{\mathbf{J} \cdot \mathbf{B}}{|\mathbf{B}|^2} = \frac{(\alpha_1 \mathbf{B}_1 + \alpha_2 \mathbf{B}_2) \cdot (\mathbf{B}_1 + \mathbf{B}_2 + \mathbf{B}_3)}{(\mathbf{B}_1 + \mathbf{B}_2 + \mathbf{B}_3) \cdot (\mathbf{B}_1 + \mathbf{B}_2 + \mathbf{B}_3)}. \tag{19}$$



**Figure 3** Minimized deviation ( $E_n$ ) vs. number of iterations for NFFF extrapolation, which decreases monotonically and saturates approximately at  $\sim 34.5\%$  for 1500 iterations.

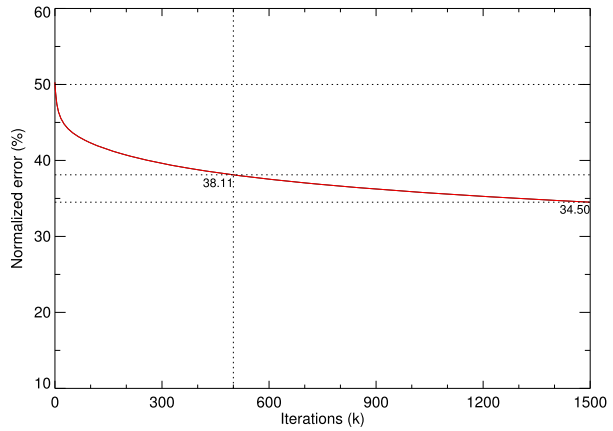


**Table 2** Averaged fractional flux error ( $\langle f_i \rangle$ ) and current weighted average of the sine of the angle between the current density and the magnetic field ( $\sigma_j$ ) for NFFF and NLFFF extrapolations.

Model	$\langle f_i \rangle$	$\sigma_j$	$\sin^{-1} \sigma_j$
NFFF	$1.11 \times 10^{-5}$	0.9123	$65.83^\circ$
NLFFF	$2.89 \times 10^{-4}$	0.1491	$8.58^\circ$

Additional to  $\alpha_1$  and  $\alpha_2$ , the twist  $\tau$  depends on the component fields. To understand the advantage, note that  $\alpha_1$  and  $\alpha_2$  for a force-free field are bounded above to ensure a monotonic decay of magnetic field strength with height from the photosphere (Nakagawa and Raadu, 1972). However, for the NFFF, the dependence of the twist on the component fields paves a way to accommodate extra twist in field lines even if the  $\alpha_1$  and  $\alpha_2$  have achieved their maximal limit.

For the purpose of quantitative and morphological comparison, the NFFF extrapolation is also carried out on the same computational grid of  $896 \times 528 \times 272$  pixels as in the NLFFF case. The variation of  $E_n$  along with the number of iterations is depicted in Figure 3, documenting a difference of 34.5% between the extrapolated and the actual transverse components.

### 3.3. Characteristics of NFFF and NLFFF Extrapolations

Following Wheatland, Sturrock, and Roumeliotis (2000), we determine the quality of the extrapolated fields by evaluating the averaged fractional flux error (Equation 20) and current-weighted average (Equation 21) of the sine of the angle between the current density and the magnetic field with their values listed in Table 2

$$\langle f_i \rangle = \left\langle \frac{(\nabla \cdot \mathbf{B})_i \Delta V_i}{B_i A_i} \right\rangle, \tag{20}$$

$$\sigma_j = \frac{\sum_i J_i \sigma_i}{\sum_i J_i}, \sigma_i = \frac{|\mathbf{J} \times \mathbf{B}|_i}{J_i B_i}, \tag{21}$$

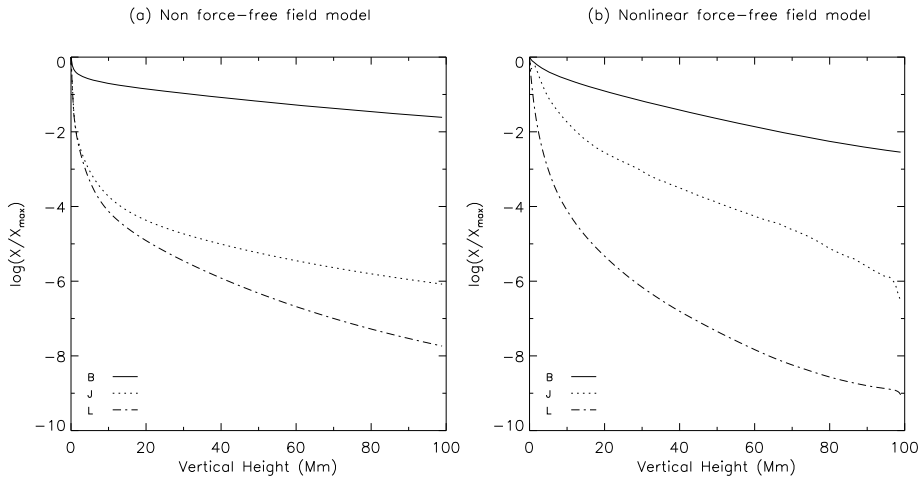


**Figure 4** Panels (a) and (b) show the variation of horizontally averaged magnetic field ( $X = B$ ), current density ( $X = J$ ), and Lorentz force ( $X = L$ ) with height on a log scale for NFFF and NLFFF models. The normalization is done using the maximum value.

where  $A_i$  is the surface area of the small volume  $\Delta V_i$ . The order of  $\langle f_i \rangle$  in both NFFF ( $\sim 10^{-5}$ ) and NLFFF ( $\sim 10^{-4}$ ) suggests that the extrapolated fields satisfy the divergence-free condition to an acceptable extent. The inverse of  $\sigma_j$  values (Table 2) measure the departure from force-free condition, which turns out to be  $\sim 65.83^\circ$  for NFFF and  $\sim 8.58^\circ$  for NLFFF. Further, Panels (a) and (b) in Figure 4 depict the logarithmic variation of horizontally averaged quantities such as magnetic field, current density, and Lorentz force with height inside the computational volume for NFFF and NLFFF extrapolations in normalized units. As expected, all the aforementioned variables decrease monotonically with height, albeit the curves are steeper for the NLFFF extrapolation.

### 3.4. Quantitative Differences

To explore the deviation of  $\mathbf{B}_{\text{NFFF}}$  from  $\mathbf{B}_{\text{NLFFF}}$ , the angle ( $\theta$ ) between the two magnetic fields is evaluated in subvolumes of extension unity in pixels. Figure 5(a) shows that the histogram plot of  $\theta$  peaks in the range  $25^\circ \leq \theta \leq 30^\circ$ , while  $\theta \leq 40^\circ$  for  $\sim 80\%$  of the computational domain. We further investigated the difference between  $\mathbf{B}_{\text{NLFFF}}$  and  $\mathbf{B}_{\text{NFFF}}$  by computing the following metric in every subvolume of the computation box:

$$d = \frac{\sum_{i=1}^3 (\mathbf{B}_{\text{NLFFF}}^i - \mathbf{B}_{\text{NFFF}}^i)^2}{|\mathbf{B}_{\text{NLFFF}}| |\mathbf{B}_{\text{NFFF}}|}, \tag{22}$$

where  $\mathbf{B}_{\text{NLFFF}}^i$  ( $i = x, y, z$ ) denotes the  $i$  component of the nonlinear force-free field and  $\mathbf{B}_{\text{NFFF}}^i$  ( $i = x, y, z$ ) denotes the  $i$  component of the nonforce-free field. The histogram plot for the corresponding metric is shown in Figure 5(b). It is seen that  $d_{\text{max}} \sim 500$  but  $d \leq 10$  for  $\sim 99.9\%$  of the computational volume.

The bottom boundary of the computational box is used to explore the differences between the observed and extrapolated magnetic fields. It is seen from Figure 5(c) that for the transverse component, the curves are almost overlapping, implying nearly identical distribution

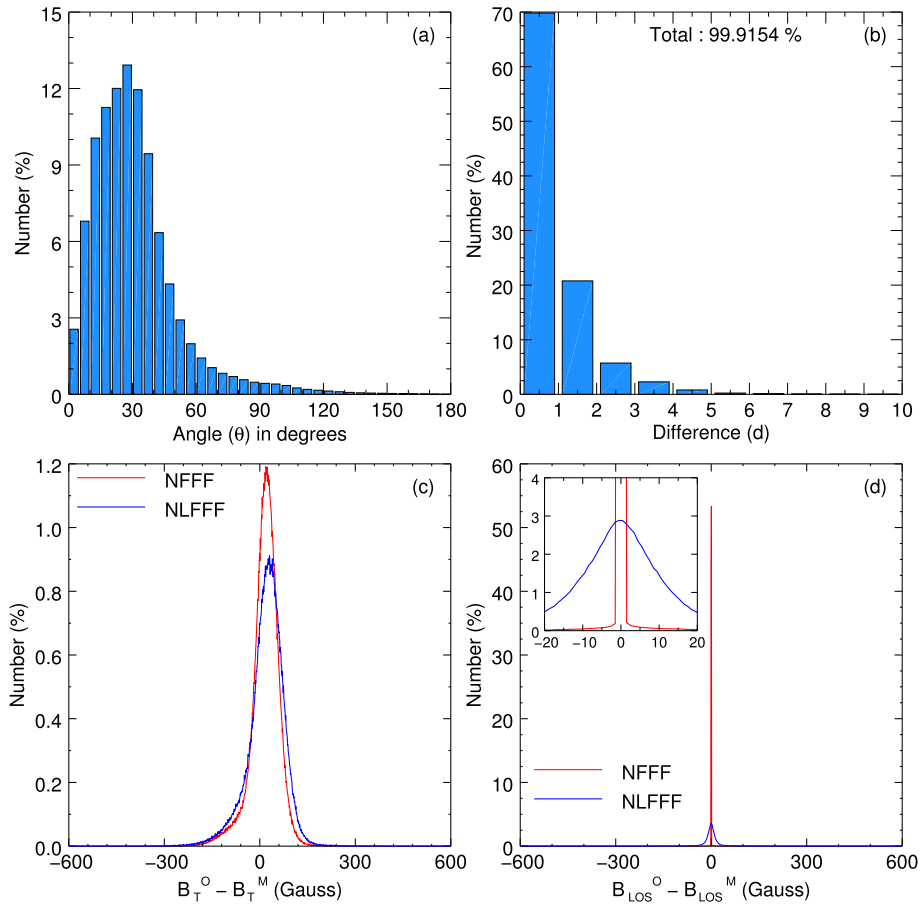


**Figure 5** (a) and (b) Histogram plot for the distribution of angular deviation ( $\theta$ ) and difference metric ( $d$ ) between the extrapolated magnetic fields,  $\mathbf{B}_{NFFF}$  and  $\mathbf{B}_{NLFFF}$ , inside the computational domain with bin size of  $5^\circ$  ( $\theta$ ) and one unit ( $d$ ), respectively. (c) and (d) Distribution of absolute difference between observed and extrapolated transverse ( $B_T$ ) and line-of-sight ( $B_{LOS}$ ) magnetic fields on the bottom boundary for NFFF (red) and NLFFF (blue). The subpanel in (d) shows the zoomed-in view of distribution for  $-20 \leq (B_{LOS}^O - B_{LOS}^M) \leq 20$ , which highlights the central peak in NLFFF when compared to NFFF. Total refers to the fraction of cells in the computational volume that fall within the range of values defined along the x-axis.

for both the extrapolation models. However, NFFF (red) shows a relatively higher peak compared to NLFFF (blue), which suggests that a greater fraction of cells satisfy the condition  $B_T^O - B_T^M \approx 0$  in NFFF extrapolation. For the line-of-sight magnetic field  $B_{LOS}$ , Figure 5(d) reveals that the distribution for NLFFF is broad, peaking at  $\sim 3\%$  (subpanel in (d)) while for NFFF, it is narrow, peaking at  $\sim 50\%$ , centered at  $B_{LOS}^O - B_{LOS}^M \approx 0$ . This suggests that the NFFF performs better than NLFFF for the line-of-sight field. The difference in distributions can also be understood in terms of a scatter plot where we calculate the Pearson correlation coefficient (R) to quantify the differences, as shown in Figures 6(a)–(d). Evidently, with  $R_{NFFF} = \{0.9226, 0.9995\}$  and  $R_{NLFFF} = \{0.8878, 0.9663\}$ , NFFF shows a better correlation to the observed line-of-sight and transverse components.

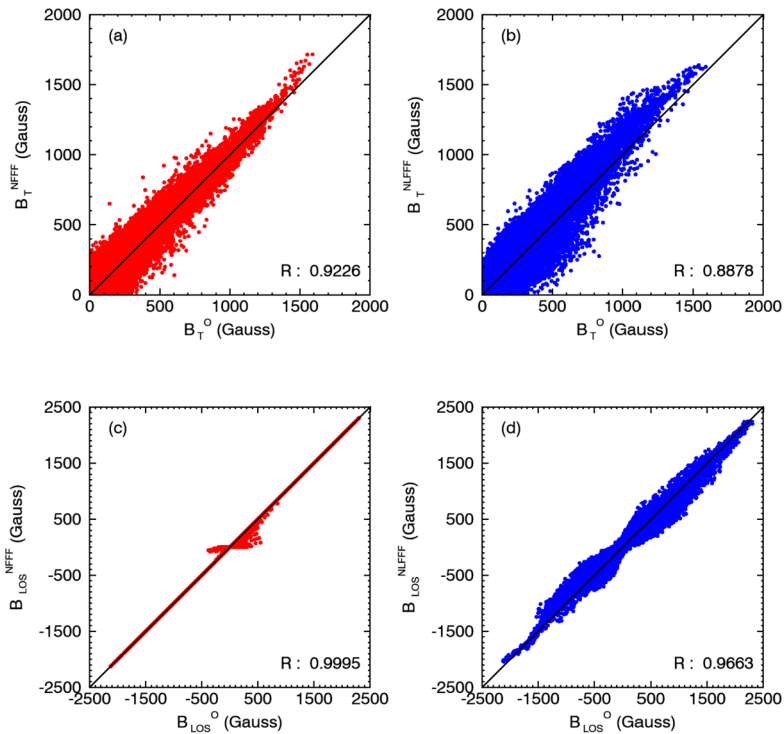


**Figure 6** The correlation between extrapolated and observed magnetic fields on the bottom boundary using scatter plots for (a) Transverse component of NFFF field, (b) Transverse component of NLFFF field, (c) line-of-sight component of NFFF field, and (d) line-of-sight component of NLFFF field.

Variations of  $\theta$  and  $d$  as a function of distance from the location of a selected null point, detected using the trilinear method (Haynes and Parnell, 2007), in both the extrapolation models are depicted in Figure 7. A similar decrease of the two parameters with distance occur for other nulls too (not shown here). From this result, we expect the possibility that regions of maximal difference between the extrapolated fields could be in the near neighborhood of magnetic nulls, which requires a detailed statistical analysis involving multiple ARs for confirmation. Since the source of energy release during eruptive events is the stored free magnetic energy, we note that the extrapolated magnetic field configuration in the NFFF model has more free magnetic energy compared to the extrapolated NLFFF, i.e.,  $E_F(\text{NFFF}) \sim 1.94 \times 10^{32}$  erg and  $E_F(\text{NLFFF}) \sim 4.34 \times 10^{31}$  erg, which implies that  $E_F(\text{NFFF}) \sim 5 \times E_F(\text{NLFFF})$ . Presumably, the difference is due to a combined effect of the faster decay of magnetic field with height in the NLFFF and higher average twist in the NFFF (not shown here).

### 3.5. Morphological Differences

To explore the morphological differences between nonforce-free and nonlinear force-free extrapolation models, we first focus on the overall *lasso* geometry. The magnetic field lines (MFLs) at large length scales, overlying the *lasso* geometry are considered to be the indicator of magnetic field configuration on the global scales, as shown in Figures 8(a) and (b) for the NFFF and NLFFF models.

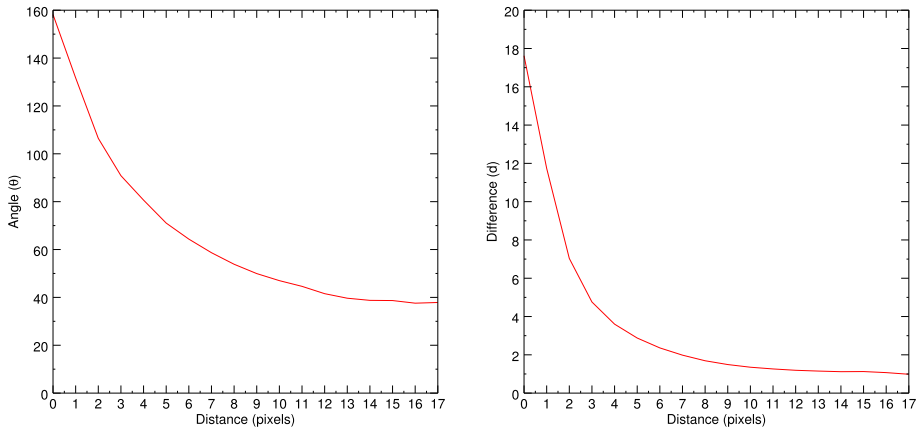


**Figure 7** Example of the variation of averaged angular deviation,  $\theta$  (left) and the averaged difference metric,  $d$ , (right) as a function of distance from the location of the detected magnetic null point in NFFF.

Two sets of high-lying (*yellow*) and low-lying (*red*) emerging MFLs, trace the *lasso* boundary, while the other end of the magnetic field lines are rooted within the area enclosed by the boundary. The overall morphology obtained in both models is aptly described by the description that magnetic field lines emerging from the noose of the *lasso* are directed toward the knot and further extend to the handle of the *lasso*. Following Liu et al. (2016), we calculate the squashing degree and find that in the near vicinity of  $b_2$  and  $b_4$ , the footpoints of red and yellow MFLs map the region of high  $\ln Q \sim 10$ , thus indicating the possibility of slipping reconnections at larger length scales. Notably, the squashing degree map for the NLFFF appears to be smudged compared to the NFFF. Auxiliary analyses (not shown here) suggest the smudging is due to the preprocessing procedure adopted in the NLFFF model.

To explore the flare dynamics in more detail, we look for the potential sites of reconnection at smaller length scales. From preliminary MHD simulations, we found multiple reconnection events spread over the spatial extent of the *lasso*. Understandably, categorizing all the reconnection sites in terms of their importance with respect to the observations is difficult and out of the scope of the present paper. For example, application of the trilinear method (Haynes and Parnell, 2007) yields multiple nulls in both extrapolated fields. Consequently, we further narrow down to those topological structures that are cospatial with the observed brightenings. The structures of interest are a hyperbolic flux tube (HFT) in the vicinity of  $b_2$  characterized by a large squashing degree and a magnetic null point in the near neighborhood of  $b_3$ . Magnetic reconnections at these locations are simulated with the dynamics being initiated from the three different initial conditions.

Using the aforementioned trilinear method, the null point in NFFF extrapolation is found to be at  $x = 588$ ,  $y = 147$ , and  $z = 18$ , while the same null point is detected at  $x = 579$ ,  $y = 153$ , and  $z = 13$  in NLFFF extrapolation; in pixel units. To illustrate various features of the null-point geometry, we manually define three positive and a negative polarity as shown in Figure 9(a) for NFFF and Figure 9(b) for NLFFF models. The polarities are labeled as  $P_1$ ,  $P_2$ ,  $P_3$ , and  $N_1$  in NFFF, while in NLFFF by the corresponding primed variables. Note that  $P'_1$  is highlighted in red, the significance of which will be explained shortly. As illustrated in Figure 10(a), for the nonforce-free field, the magnetic field lines originating from  $P_1$ ,  $P_2$ , and  $P_3$  terminate at  $N_1$ , thus constituting the dome-shaped fan surface (*red* MFLs) and the lower spine ( $S_1$ ) of the null, while the *white* MFLs, originating from  $P_1$ ,  $P_2$ , and

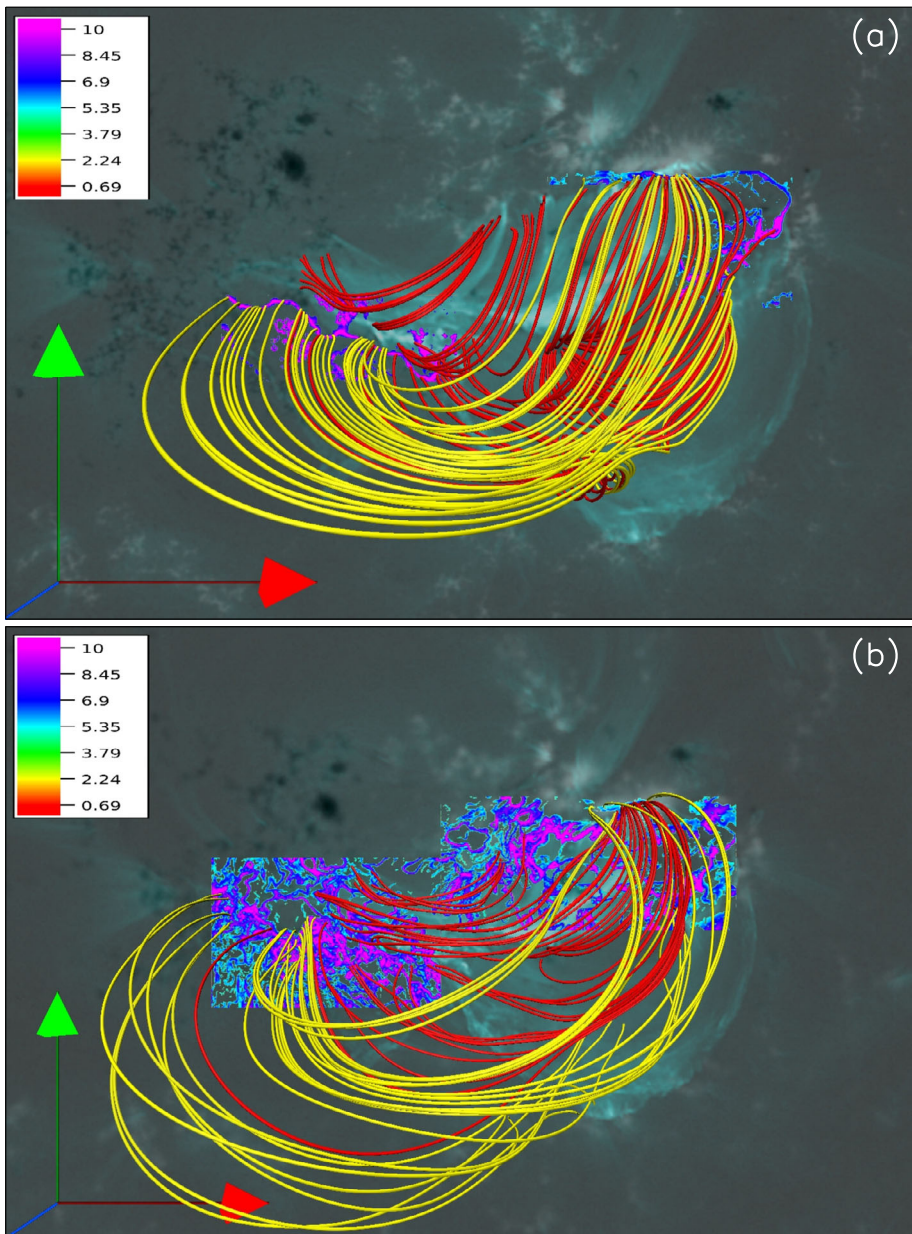


**Figure 8** Panels (a) and (b): Top side view of the global MFL morphology in NFFF and NLFFF modeling. Two sets (*red* and *yellow*) of magnetic field lines are overlaid on top of the line-of-sight magnetogram along with the *lasso* structure identified in the 131 Å channel of SDO/AIA at 02:59:56 UT (Figure 2). The regions of high gradient in magnetic field line connectivity are shown using the map of the calculated squashing degree ( $\ln Q$ ) distribution on the bottom boundary, with the coded color table. The *red*, *green*, and *blue* arrows mark the *x*-, *y*-, and *z*-directions, respectively.

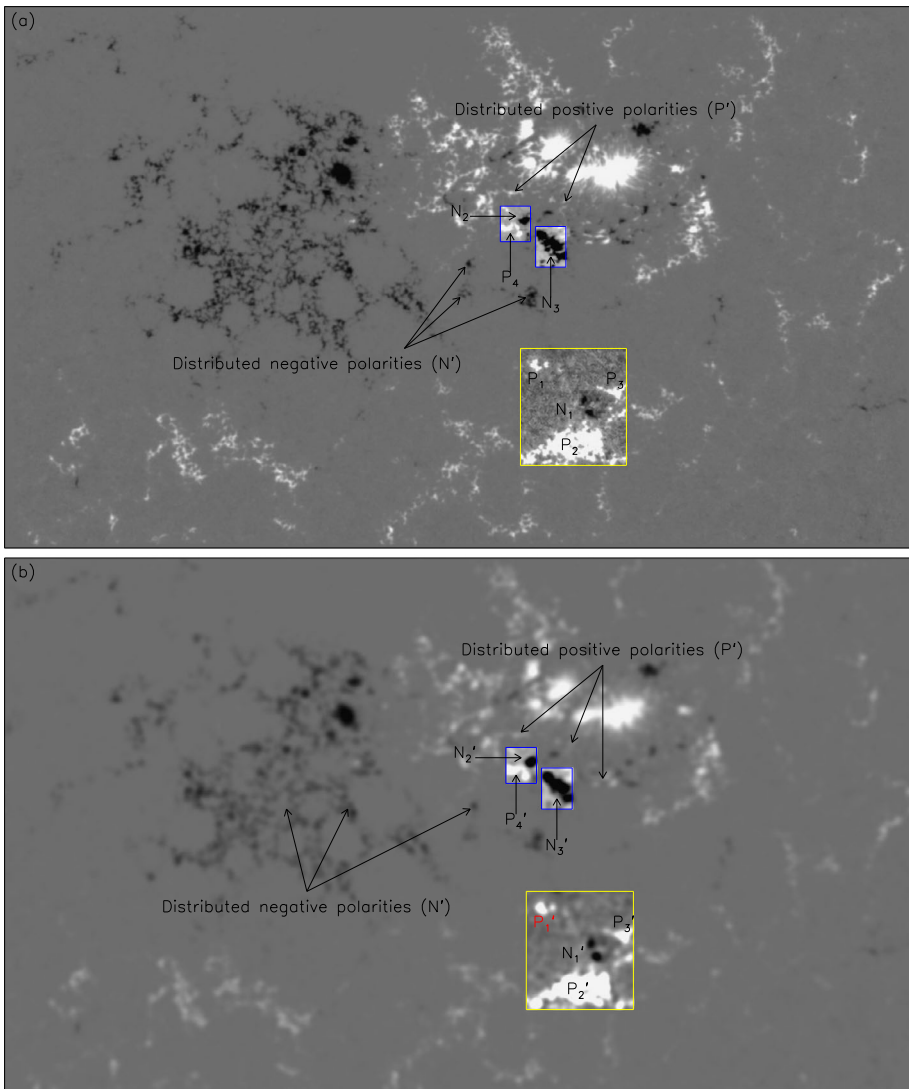


**Figure 9** Panels (a) and (b) Distribution of  $B_{LOS}$  over the photospheric boundary in nonforce-free and nonlinear force-free modeling. The images are scaled for  $|B_{LOS}| \leq 1000$  G in (a)  $|B_{LOS}| \leq 1500$  G in (b). The yellow box enclosing polarities  $P_1, P_2, P_3,$  and  $N_1$  in (a) and the corresponding primed polarities in (b) constitute the null-point topology. The magnetic polarities  $P_4$  and  $N_2$  within the blue box along with distributed polarities (P and N) in (a) and the corresponding primed polarities in (b) comprise the HFT geometry. The additional polarity  $N_3(N_3')$  in (a) and (b) will be used to describe the field-line dynamics at HFT during the simulated evolution. The regions within the yellow and blue boxes are scaled further for enhanced visibility.

$P_3$  and extending into the corona, form the upper spine ( $S_2$ ) of the null. For the nonlinear force-free field, Figure 10(b) depicts a similar magnetic null-point morphology with identifiable fan surface, upper and lower spines. Despite the apparent similarity of the null-point topology as obtained in the two models, we note a crucial difference regarding the relevance of  $P_1'$ . It is seen that there is no recognizable magnetic field line connectivity between the

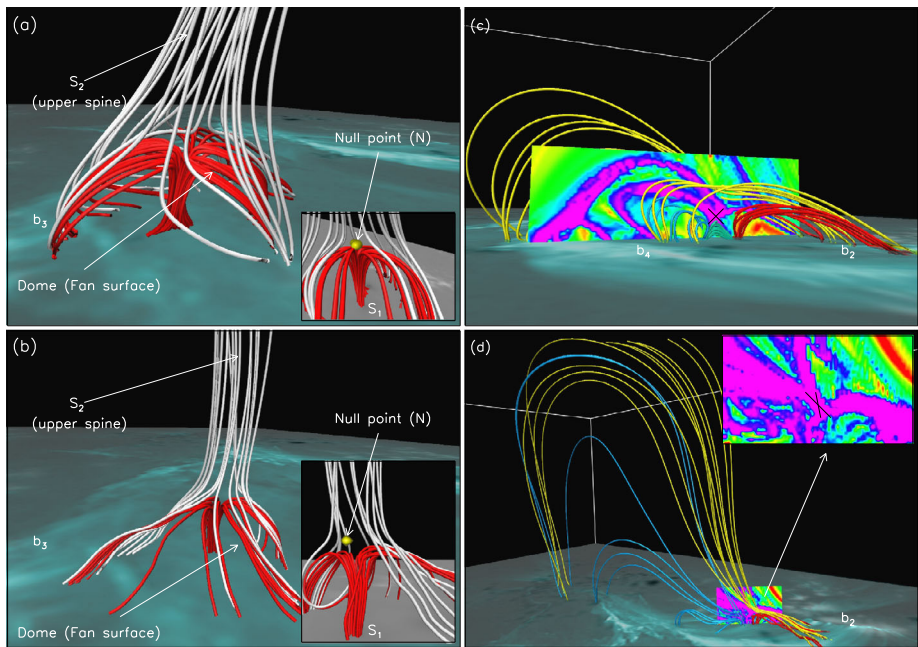


**Figure 10** Panels (a) and (b): Magnetic null-point topology in nonforce-free and nonlinear force-free extrapolation models, depicting the dome-shaped fan surface (red), lower spine (red;  $S_1$ ), and upper spine (white;  $S_2$ ). The subpanels in (a) and (b) highlight the null-point location (yellow). Panels (c) and (d): Hyperbolic flux tube morphology in NFFF and NLFFF extrapolation models along with  $\ln Q$  distribution in a plane perpendicular to the bottom boundary.

polarities  $P'_1$  and  $N'_1$ . This particular difference could be due to the preprocessing adopted in NLFFF modeling, thus effectively destroying the connectivity of  $P'_1$  with respect to  $N'_1$ .

The magnetic field lines constituting the hyperbolic flux tube (Titov, Hornig, and Démoulin, 2002) can be categorically separated into four distinct connectivity domains (Pariat, 2020), such that the field lines inside each domain share similar field-line connectivity. To specify the various domains, we manually define magnetic polarities as  $P_4(P'_4)$  and  $N_2(N'_2)$  along with extended regions of distributed positive and negative regions— $P(P')$  and  $N(N')$ , as shown in Figure 9(a) for the nonforce-free field and Figure 9(b) for the nonlinear force-free field. Four different sets of MFLs (green, yellow, blue, and red) comprising the HFT morphology in NFFF are depicted in Figure 10(c), where each set of MFL is analogous to a connectivity domain. We further note the presence of quasiseparatrix layers (QSL) present in the HFT geometry. The green and blue MFLs originating from  $P_4$  constitute a QSL whose footpoints terminate at  $N_2$  and  $N$ , respectively. Another QSL is defined by the set of red and yellow MFLs originating from  $P$  and terminating at  $N_2$  and  $N$ . The intersection of the two identified QSLs results in the formation of HFT. Similarly, for the nonlinear force-free field, we obtain a similar morphology, as shown in Figure 10(d) but with two subtle differences. Comparison of Panels (c) and (d) reveals that the counterpart of green MFLs (in NFFF) is not found in NLFFF, which could be due to the weaker correlation of the nonlinear force-free field with the observed line-of-sight magnetic field. Further, it is seen that the terminating footpoints of yellow and blue MFLs are more scattered in NLFFF, extending more towards the handle of the lasso. The map of calculated squashing degree in the plane perpendicular to the bottom boundary reveals a characteristic X-shape for the distributed  $\ln Q$  ( $\sim 10$ )



values in both the models, thus supporting our interpretation of the MFL morphology. We mark an additional negative polarity— $N_3(N'_3)$ , whose significance will be explained later in the context of simulated evolution.

For the chosen magnetic null-point and hyperbolic flux tube morphologies, the effect of such similarities and differences on the fundamental process of magnetic reconnection is explored with the simulated evolution, as described in the following sections.

#### 4. Numerical Model

The key to a successful numerical simulation of solar transients is to keep MRs localized at the plausible sites, while allowing for the condition of flux freezing to hold good elsewhere. The coronal plasma is idealized to be a thermodynamically inactive, incompressible magnetofluid having infinite electrical conductivity. The governing dimensionless MHD equations are

$$\frac{\partial \mathbf{v}}{\partial t} + (\mathbf{v} \cdot \nabla) \mathbf{v} = -\nabla p + (\nabla \times \mathbf{B}) \times \mathbf{B} + \frac{1}{R_F^A} \nabla^2 \mathbf{v}, \quad (23)$$

$$\frac{\partial \mathbf{B}}{\partial t} = \nabla \times (\mathbf{v} \times \mathbf{B}), \quad (24)$$

$$\nabla \cdot \mathbf{v} = 0, \quad (25)$$

$$\nabla \cdot \mathbf{B} = 0, \quad (26)$$

where  $R_F^A = (V_A L)/\nu$  is an effective fluid Reynolds number with  $V_A$  as the Alfvén speed and  $\nu$  as the kinematic viscosity. Hereafter,  $R_F^A$  is referred to as the fluid Reynolds number to keep the terminology uncluttered. The dimensionless equations are obtained by the normalizations listed below:

$$\mathbf{B} \rightarrow \frac{\mathbf{B}}{B_0}, \mathbf{v} \rightarrow \frac{\mathbf{v}}{V_a}, L \rightarrow \frac{L}{L_0}, t \rightarrow \frac{t}{\tau_a}, p \rightarrow \frac{p}{\rho_0 V_A^2}. \quad (27)$$

In general,  $B_0$  and  $L_0$  are characteristic values of the system under consideration. The constant mass density is denoted as  $\rho_0$ . Equations 23–26 are solved by the numerical model EULAG-MHD (Smolarkiewicz and Charbonneau, 2013)—a model based on an earlier hydrodynamic model EULAG, mostly used in atmospheric and climate research (Prusa, Smolarkiewicz, and Wyszogrodzki, 2008). The magnetic field component  $B_z$  is kept fixed at the bottom boundary while all other boundaries are treated as open. For the velocity, all boundaries are treated as open. The incompressibility condition (Equation 25) is applied on the integral form of the momentum equation (Equation 23) to generate an elliptic boundary value problem for the pressure  $p$ ; cf. Bhattacharyya, Low, and Smolarkiewicz, 2010 and the references therein. Importantly, the pressure adjustments at every time step being instantaneous, the numerical model does not support acoustic modes of MHD waves that depend on kinetic pressure variations for propagation. Similarly, an auxiliary potential in the induction equation (Equation 24) is added and an identical procedure is invoked to keep  $\mathbf{B}$  solenoidal (see Smolarkiewicz and Charbonneau, 2013 and Ghizaru, Charbonneau, and Smolarkiewicz, 2010 for details). In the following, features important to our simulations are only mentioned, while the details can be found in Smolarkiewicz and Charbonneau (2013) and references therein. The model is based on the spatiotemporally second-order

accurate nonoscillatory forward-in-time multidimensional positive-definite advection transport algorithm (MPDATA: Smolarkiewicz, 2006). A characteristic of MPDATA employed extensively in our simulation is its proven numerical dissipative property, which, intermittently and adaptively, regularizes the underresolved scales by simulating MRs and mimicking the action of explicit subgrid-scale turbulence models (Margolin, Rider, and Grinstein, 2006) as in the Implicit Large Eddy Simulations (ILESs: Grinstein, Margolin, and Rider, 2007). Prior works relying on these ILES-assisted magnetic reconnections (MRs) have successfully simulated the source-region dynamics of various solar flares (Kumar et al., 2016, Prasad et al., 2018, Nayak, Bhattacharyya, and Kumar, 2021). In this paper also, we continue with the ILES-assisted MRs.

To optimize computational cost, the active-region cutout is remapped on a coarser grid having  $448 \times 256 \times 192$  pixels resolved on a computational grid of  $x \in [-0.875, 0.875]$ ,  $y \in [-0.5, 0.5]$ , and  $z \in [-0.375, 0.375]$ , in a Cartesian coordinate system. The spatial step sizes are  $\Delta x = \Delta y = \Delta z \approx 0.0039$  ( $\approx 723$  km), while the time step is  $\Delta t = 2 \times 10^{-3}$ . The mass density is set to  $\rho_0 = 1$ . Further, the fluid Reynolds number is set to 5000, which is five times smaller than the coronal value of  $\approx 25000$ . The coronal value is calculated using kinematic viscosity,  $\nu = 4 \times 10^9 \text{ m}^2 \text{ s}^{-1}$  (Aschwanden, 2005, p. 791) in the solar corona. A reduced  $R_F^A$  can be interpreted as a smaller computed Alfvén speed where  $V_A|_{\text{computed}} \approx 0.14 \times V_A|_{\text{corona}}$ . The Alfvén speeds are estimated with 139.2 Mm (the active-region scale) as the characteristic scale for the computational domain and 100 Mm for the typical corona. The simulation time is  $1000\Delta t$ , which, with  $\tau_A \approx 9.68 \times 10^2 \text{ s}$ , approximately equals an observation time of  $\approx 33$  minutes. Presumably, a smaller Reynolds number only slows down the dynamics without altering other characteristics of reconnection and thus saves computational cost, as realized in a recent work by Jiang et al. (2016).

## 5. Simulated Dynamics

Three distinct simulations (hereafter referred as  $S_1$ ,  $S_2$ , and  $S_3$ ) are performed starting from different choices of the initial configuration. Because of the large coverage of the magnetogram, we chose to perform simulations with reduced resolution on a computational grid of dimensions  $448 \times 256 \times 192$ . All the simulations are initiated by utilizing the vector magnetogram observed at 02:48:00 UT. The reduction in resolution is checked to have no effects on the identified topological structures. Simulation  $S_1$  takes NFFF as the input magnetic field with nonzero Lorentz force in the computational volume, initialized from a motionless state or with zero external flow. Initially, the Lorentz force pushes the plasma to generate dynamics. In simulation  $S_2$ , the NLFFF is driven only by the residual force due to numerical deviation from its analytical value of exactly zero. For the simulation  $S_3$ , we further impose a perturbative flow to  $S_2$ , derived from the 100th timestep of  $S_1$ . For brevity, hereafter the three initial conditions are referred to as  $S_1 \equiv \{\mathbf{B}_{\text{NFFF}}, \mathbf{0}\}$ ,  $S_2 \equiv \{\mathbf{B}_{\text{NLFFF}}, \mathbf{0}\}$ , and  $S_3 \equiv \{\mathbf{B}_{\text{NLFFF}}, \mathbf{v}_{\text{pert}}\}$ . With these simulations, we explore the underlying magnetic reconnection at the magnetic null point and at the hyperbolic flux tube (HFT). Importantly, in all the simulations we find magnetic null-point generation and annihilation (the null is named as a transient null or TN) in the near neighborhood of the HFT. Using the trilinear method of null-point detection, we confirm the presence of this magnetic null point (TN) and obtain the null-point coordinates (pixel units), as shown in Table 3. The next section details the simulation results.

**Table 3** Coordinates of the transient magnetic null point as detected in  $S_1$ ,  $S_2$ , and  $S_3$  by the trilinear method of null-point detection.

	$S_1$	$S_2$	$S_3$
x	247.	259.	259.
y	144.	155.	157.
z	1.	4.	6.

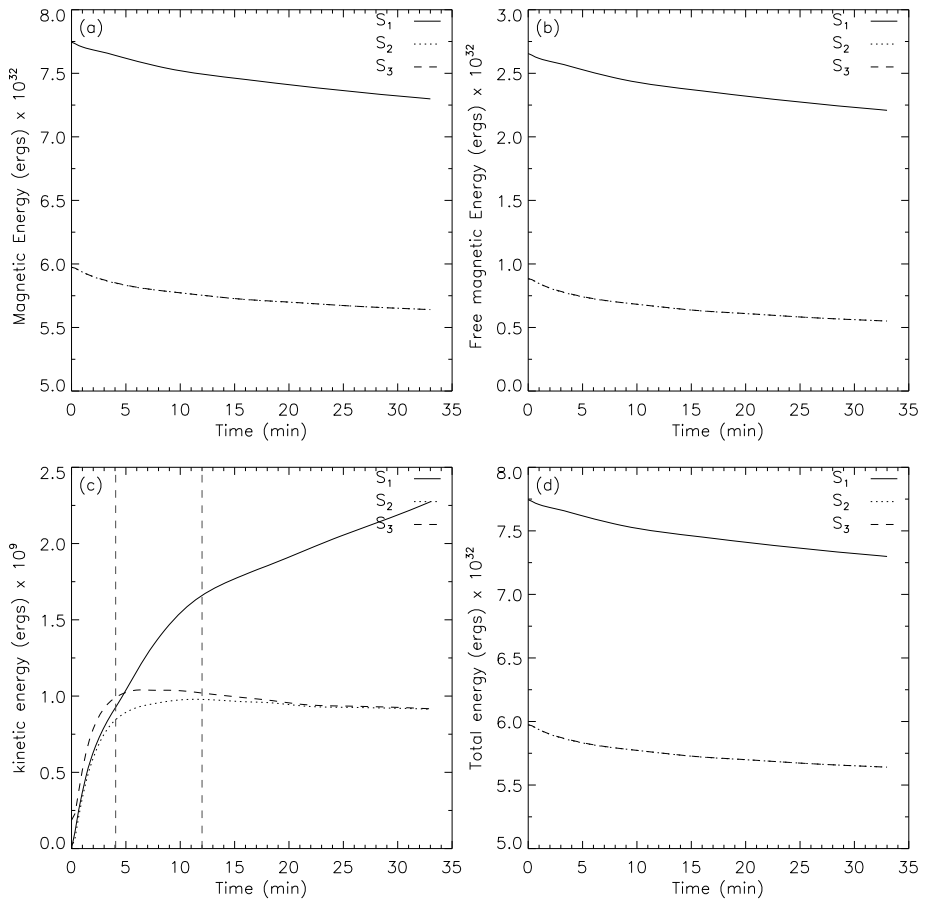


**Figure 11** Panels (a), (b), (c), and (d) depict the time evolution of magnetic energy, free magnetic energy, kinetic energy, and total energy (magnetic + kinetic) sum for simulations  $S_1$  (solid line),  $S_2$  (dotted line), and  $S_3$  (dashed line), respectively. The x- and y-axis represent time (minutes) and energy (ergs) in physical units. The dashed blue lines correspond to instances of a change in slope of the kinetic energy profile for  $S_1$ .

### 5.1. Global Energetics

The global-scale dynamics is investigated by exploring the evolution of volume-integrated magnetic, free magnetic, kinetic, and total (magnetic + kinetic) energies; depicted in Panels (a), (b), (c), and (d) of Figure 11. The solid, dotted, and dashed lines correspond to simulations  $S_1$ ,  $S_2$ , and  $S_3$ . Panels (a) and (b) establish a similar behavior of magnetic and free

magnetic energies in all the three simulations—exhibiting a continuous decrease with time and plots being parallel to each other; albeit starting from different initial values. Noticeably, the plots for simulations  $S_2$  and  $S_3$  overlap, being almost indistinguishable. The free energies at the initial states are  $2.65 \times 10^{32}$  ergs in  $S_1$  and  $8.8 \times 10^{31}$  ergs in  $S_2$  and  $S_3$ . The changes in free energies over the simulation, covering the flare duration, are of the order  $4.46 \times 10^{31}$  in  $S_1$  and  $3.33 \times 10^{31}$  ergs in the other two—presumably consistent with the range of upper C-class to M-class flares (Rempel, Cheung, and Chintzoglou, 2021). Interestingly, the decreases in total magnetic energy (Panel (a)) in all three simulations are approximately equal. For  $S_1$  the decrease is 5.76%, while it is 5.58% in  $S_2$  and  $S_3$ , agreeing with the idea put forward in the Introduction. Moreover, the residual magnetic energy after relaxation is still much higher than the potential energy ( $\sim 5.09 \times 10^{32}$  ergs), hence the active region, in principle, can still produce additional flares, as envisioned in Mitra et al. (2018). Contrary to the free magnetic energy, the variation of kinetic energy with time shows a different behavior for  $S_1$  when compared to  $S_2$  or  $S_3$ . For the simulation initiated with NFFF, the Lorentz force is not balanced entirely over the simulation period and the kinetic energy exhibits an increasing profile throughout the simulation time. Furthermore, we note a change in the slope of the kinetic energy plot for  $S_1$  at two distinct points (marked by *dashed blue lines*)—first at  $\sim 4$  min. ( $\equiv 02:52:00$  UT) and then at  $\sim 12$  min ( $\equiv 03:00:00$  UT), which agrees approximately with instances of the observed brightenings, illustrated in Panels (b) and (c) of Figure 2. For simulations  $S_2$  and  $S_3$ , initiated with the NLFFF, the system relaxes to an approximate steady state (in kinetic energy), as is evident from Panel (c). During the initial phase, the kinetic energy in  $S_3$  is higher than  $S_2$ , which is due to the perturbative flow. The sums of magnetic energy and the kinetic energy in all the three simulations behave similarly and decreases monotonously with time, as shown in Panel (d).

## 5.2. Magnetic Null Point

We focus on the changes in various magnetic field line connectivities because of reconnection, during the simulated evolution of null-point topology. The left column in Figure 12 depicts the evolution of various MFLs constituting the fan surface (*red*) and spine structures (*white*) for  $S_1$ . Among the selected field lines, the first instance of magnetic reconnection at the null-point location occurs at  $t = 270$  ( $\sim 8m54s \equiv 02:56:54$  UT), as shown in Panel (b), where one of the red MFL constituting the lower spine ( $S_1$ ) changes its connectivity from the photospheric boundary to that of an open field line. Furthermore, during this time window, the fan plane is seen to exhibit slipping reconnection (see the corresponding animations), which traces the brightening  $b_3$ , thus correlating well with the observed temporal sequence of  $b_3$  (Panels (c) and (d) in Figure 2). The aforementioned, null point and slipping reconnections, continue until about  $t = 500$  ( $\sim 16m30s \equiv 03:04:30$  UT), where the lower spine ( $S_1$ ) is missing, suggesting that all the red MFLs forming the lower spine have reconnected at the null point. Coincidentally, the corresponding time agrees precisely with the peak time of the flare  $\equiv 03:04:08$  UT. Toward the end of simulation  $S_1$ , small circular motions along the footpoints of *red* and *white* MFLs (see animations) constituting the fan plane relax the overall magnetic field configuration in the local neighborhood of the null point. Panel (d) in Figure 12 depicts the final state of simulated null-point topology at  $t = 1000$  ( $\sim 33m \equiv 03:21:00$  UT), characterized by open magnetic field lines emerging from  $P_1$ ,  $P_2$ , and  $P_3$ .

Simulations utilizing the nonlinear force-free field as input magnetic field,  $S_2$  and  $S_3$  are analyzed and selective instances from the field-line evolution in null-point topology

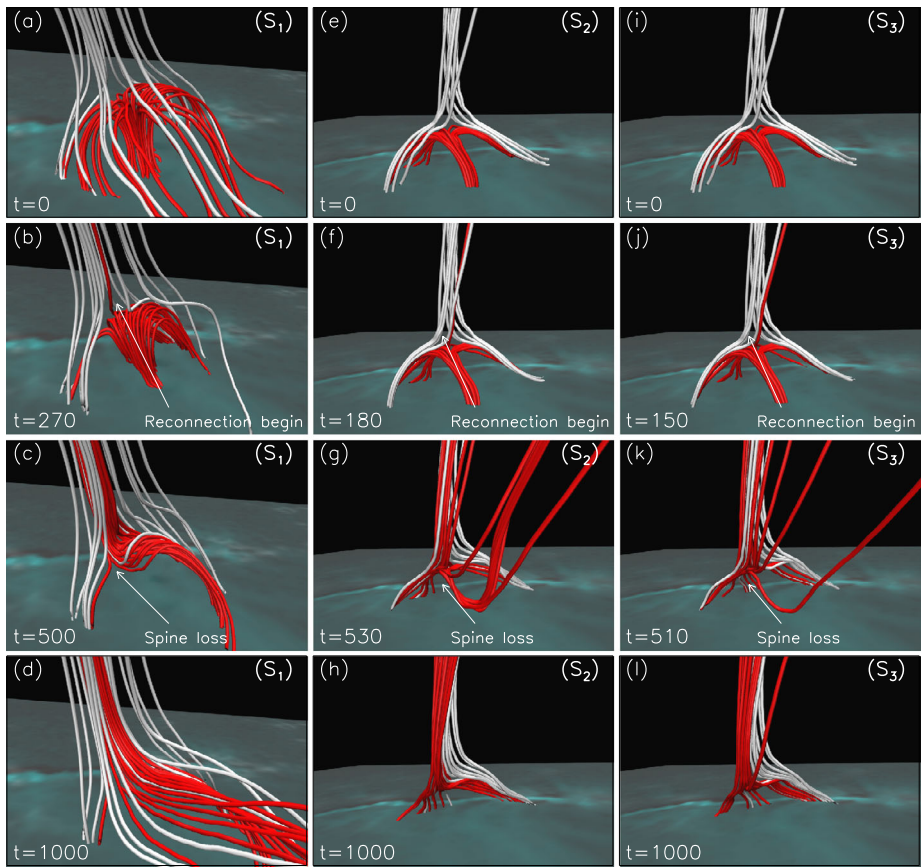


**Figure 12** Snapshots from the simulated evolution of magnetic field lines in null-point topology for  $S_1$  (left column),  $S_2$  (middle column), and  $S_3$  (right column). The second row depicts the first instance of magnetic reconnection at the null-point location, while the third row corresponds to the loss of the lower spine. The copatiality of the observed brightening  $b_3$  and the null-point topology can be seen from the overlaid line-of-sight magnetogram from SDO/HMI at 02:48 UT along with an image of the flaring region from SDO/AIA in the 131 Å channel at 02:59:56 UT on the bottom boundary (animations available).

are presented in the middle ( $S_2$ ) and right ( $S_3$ ) columns of Figure 12. The first instance of magnetic reconnection at the null-point location is seen at  $t = 180$  (Figure 12(f)) in  $S_2$ , while in  $S_3$ , the same occurs at  $t = 150$  (Figure 12(j)), presumably due to the presence of finite perturbative flow. Counterintuitively, the reconnection in  $S_2$  occurs earlier than in  $S_1$ , which may be accredited to the fact that the null-point topology in the two extrapolation models are similar and not identical. As more and more magnetic field lines reconnect at the null point, the lower spine is lost at  $t = 530$  (Figure 12(g)) in  $S_2$ , while the same occurs at  $t = 510$  (Figure 12(k)) in  $S_3$ . Interestingly, the lower spine is seen to disappear in all the simulations, nearly around the same time instance. In close correspondence with simulation  $S_1$ , the final state in  $S_2$  and  $S_3$ , at  $t = 1000$  is also identified by open magnetic field lines emerging from  $P'_2$  and  $P'_3$ , as shown in Panels (h) and (l), respectively. For all the simulations, various changes in the magnetic field line connectivity due to reconnection at the null-point topology, are summarized in Table 4.

**Table 4** Summary of the footpoint mapping, before and after reconnection, corresponding to the magnetic null-point topology for simulations  $S_1$ ,  $S_2$ , and  $S_3$ .

	Before reconnection	After reconnection
$S_1$	$P_1, P_2, P_3 \rightarrow N_1$	$P_1, P_2, P_3 \rightarrow \text{open}$
$S_2$	$P'_2, P'_3 \rightarrow N'_1$	$P'_2, P'_3 \rightarrow \text{open}$
$S_3$	$P'_2, P'_3 \rightarrow N'_1$	$P'_2, P'_3 \rightarrow \text{open}$

### 5.3. Hyperbolic Flux Tube

The magnetic field line dynamics at the location of hyperbolic flux tube (HFT) is complex, exhibiting multiple reconnection events for each set of MFL. To simplify the analysis, rather than considering the overall dynamics at the HFT, we focus on each MFL set separately. Further, due to the absence of *green* field lines in the nonlinear force-free field extrapolation, we consider only *yellow*, *red*, and *blue* MFLs for comparison across the three simulations. Additionally, due to frequent changes associated with the field-line connectivity during reconnection, we limit ourselves to the peak time of the flare, which corresponds to  $t = 500$  in the simulated evolution. The relation between simulated time and peak time of the flare is estimated by calculating the time in seconds corresponding to one unit time step in the numerical simulations ( $\sim 19.8$  s).

During the simulated evolution, the reconnection assisted changes, in the field-line dynamics of *yellow* MFLs, are depicted in Figure 13 for  $S_1$  (*left*),  $S_2$  (*middle*), and  $S_3$  (*right*) columns. Panels (a), (d), and (g) show the initial geometrical configuration, characterized by field-line mapping between the polarity pairs (P, N) for  $S_1$  and (P', N') for the other two simulations. The MHD evolution of plasma leads to magnetic reconnection and we break the entire sequence of changes in connectivity into three distinct parts. First, we find that a few of the selected field lines change their mapping from N to  $N_3$  in  $S_1$ , as shown by Panel (b) at  $t = 310$  and from  $N'$  to  $N'_3$  in  $S_2$  and  $S_3$ , as shown by Panels (e) and (h) at  $t = 230$  and  $t = 180$ , respectively (Table 5). Interestingly, reconnection in  $S_2$  occurs earlier than in  $S_1$ , similar to what we found in the null-point topology also. Secondly, we note connectivity changes in the reverse order, i.e., from  $N_3$  to N for  $S_1$  and from  $N'_3$  to  $N'$  for simulations  $S_2$  and  $S_3$ , as depicted by Panel (c), (f), and (i) at  $t = 500$ . Consequently, the aforementioned changes can be summarized to follow  $N(N') \rightarrow N_3(N'_3) \rightarrow N(N')$  (Table 5) for all the initial conditions. Thirdly, certain field lines, rooted in the N(N') polarities exhibit slipping reconnection in all the three simulations (see animations), which leads to a small shift in the footpoints across regions (pink patches at the bottom boundary) of high squashing degree ( $\ln Q \sim 10$ ). The slipping motions partially map the brightenings  $b_2$  and  $b_4$ , thus contributing toward the observed transient activity.

Next, we explore the dynamics of the *red* colored MFL set illustrated in Figure 14. The MFLs follow a sequence of complex changes owing to a combined effect of reconnection and fluid advection. The initial morphological arrangements for the three initial fields are shown in Panels (a), (d), and (g) of the same figure. The morphologies are characterized by field-line connectivity between the polarity pairs (P,  $N_2$ ) for  $S_1$  and (P',  $N'_2$ ) for the other two initial fields. As reconnection ensues, we note changes in footpoint mapping for a few field lines from  $N_2$  to N in  $S_1$ , as shown in Panel (b) at  $t = 10$  and from  $N'_2$  to  $N'$  in  $S_2$  and  $S_3$ , as depicted in Panels (e) and (h) at  $t = 50$  and  $t = 40$ , respectively (Table 5). Following this, we find small changes, facilitated by advection, thus causing some minor but identifiable shift in footpoint connectivity from  $N_2(N'_2)$  toward  $N_3(N'_3)$ , across all the simulations (see the corresponding animations). The advection is distinguished from slipping reconnection based on the continuity of field-line movement over the photospheric boundary and the

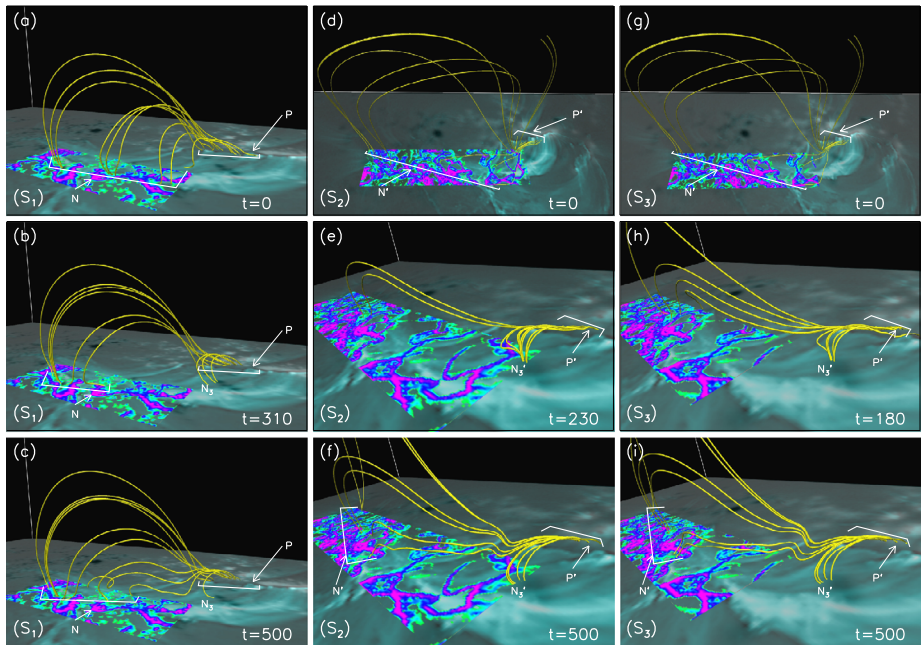


**Figure 13** Snapshots from the simulated evolution of *yellow* magnetic field lines in the hyperbolic flux tube (HFT) morphology for  $S_1$  (left column),  $S_2$  (middle column), and  $S_3$  (right column). The *first* row depicts the initial field-line configuration, the *second* row shows the change in footpoint mapping from  $N(N') \rightarrow N_3(N'_3)$ , while the *third* row corresponds to the change  $N_3(N'_3) \rightarrow N(N')$ . To analyze the associated slipping reconnection, the distribution of  $\ln Q$  is shown on the bottom boundary with the same color coding as in Figure 8. The cospatiality of observed brightening  $b_2$  with the HFT can be seen from the overlaid line-of-sight magnetogram from SDO/HMI at 02:48 UT along with an image of AR11977 from SDO/AIA in the 131 Å channel at 02:59:56 UT on the bottom boundary (animations available).

low value of the squashing degree in that region. Subsequently, another occurrence of reconnection is identified, producing a change in connectivity toward the polarity  $N$  in  $S_1$ , as shown in Panel (c) at  $t = 460$  and toward  $N'$  in simulations  $S_2$  and  $S_3$ , as shown in Panels (f) and (i) at  $t = 390$  and  $t = 370$ , respectively. All the aforementioned changes, because of reconnection in the field-line dynamics of red MFLs, can be summarized into the sequence  $N_2(N'_2) \rightarrow N(N') \rightarrow$  advection  $\rightarrow N(N')$ , which is preserved in all the simulations. Additionally, we note slipping reconnection in the  $P(P')$  region during the course of evolution (see the corresponding animations), thus contributing to the observed brightening  $b_2$ .

Finally, we look at the field-line dynamics in the set of *blue* magnetic field lines. In particular, for this set of MFLs, we note that slipping reconnections dominate the entire simulated evolution. To begin with, the initial magnetic field line configuration at  $t = 0$  is depicted in Figure 15, identified by field-line connectivity between the polarity pairs ( $P_4, N$ ) for  $S_1$  and ( $P'_4, N'$ ) for the other two simulations, as shown in Panels (a), (d), and (g), respectively. Over time, slipping reconnection sets in (see animations), thus transforming the initial configuration. The first significant change is noted where the footpoint mapping of a few magnetic field lines change from  $P_4$  to  $P$  in  $S_1$ , as shown in Panel (b) at  $t = 210$  and from  $P'_4$  to  $P'$  in simulations  $S_2$  and  $S_3$ , as depicted in the corresponding Panels (e) and (h) at  $t = 140$  and  $t = 120$  (Table 5). The final morphological organization of the *blue* MFLs at  $t = 500$  is characterized by the field-line connectivity between the polarity pair ( $P, N$ ) in simulation  $S_1$ , as

**Table 5** Summary of the footpoint mapping corresponding to *yellow*, *red*, and *blue* magnetic field lines in the hyperbolic flux tube morphology for simulations  $S_1$ ,  $S_2$ , and  $S_3$ . The round brackets denote the precise number of selected magnetic field lines between the specified polarities, while the *arrows* indicate the direction of the field line. The *left* ( $t = 0$ ), *middle* ( $t = t_1$ ), and *right* ( $t = t_2$ ) columns represent the initial state, first, and second instances of significant changes in the connectivity of field lines. Note that  $t_1$  and  $t_2$  are variables depending on the set of magnetic field lines under consideration.

	$t = 0$	$t = t_1$	$t = t_2$
<b>Yellow</b>			
$S_1$	$P \rightarrow N$ (10)	$P \rightarrow N$ (6), $P \rightarrow N_3$ (4); $t = 310$	$P \rightarrow N$ (9), $P \rightarrow N_3$ (1)
$S_2$	$P' \rightarrow N'$ (10)	$P' \rightarrow N'$ (2), $P' \rightarrow N'_3$ (8); $t = 230$	$P' \rightarrow N'$ (6), $P' \rightarrow N'_3$ (4)
$S_3$	$P' \rightarrow N'$ (10)	$P' \rightarrow N'$ (5), $P' \rightarrow N'_3$ (5); $t = 180$	$P' \rightarrow N'$ (6), $P' \rightarrow N'_3$ (4)
<b>Red</b>			
$S_1$	$P \rightarrow N_2$ (15)	$P \rightarrow N$ (1), $P \rightarrow N_2$ (14); $t = 10$	$P \rightarrow N$ (1), $P \rightarrow N_2$ (7) $P \rightarrow N_3$ (6), $P_4 \rightarrow N_3$ (1) $t = 470$
$S_2$	$P' \rightarrow N'_2$ (15)	$P' \rightarrow N'$ (2), $P' \rightarrow N'_2$ (13); $t = 50$	$P' \rightarrow N'$ (3), $P' \rightarrow N'_2$ (6) $P' \rightarrow N'_3$ (6); $t = 390$
$S_3$	$P' \rightarrow N'_2$ (15)	$P' \rightarrow N'$ (1), $P' \rightarrow N'_2$ (14); $t = 40$	$P' \rightarrow N'$ (3), $P' \rightarrow N'_2$ (6) $P' \rightarrow N'_3$ (6); $t = 370$
<b>Blue</b>			
$S_1$	$P_4 \rightarrow N$ (10)	$P_4 \rightarrow N$ (6), $P \rightarrow N$ (4); $t = 210$	$P \rightarrow N$ (10); $t = 500$
$S_2$	$P'_4 \rightarrow N'$ (10)	$P'_4 \rightarrow N'$ (5), $P' \rightarrow N'$ (5); $t = 140$	$P' \rightarrow N'$ (10); $t = 560$
$S_3$	$P'_4 \rightarrow N'$ (10)	$P'_4 \rightarrow N'$ (5), $P' \rightarrow N'$ (5); $t = 120$	$P' \rightarrow N'$ (10); $t = 560$

shown in Panel (c), while the same mapping between polarity pair ( $P'$ ,  $N'$ ) is found in simulations  $S_2$  and  $S_3$  at  $t = 560$ , as shown in Panels (f) and (i). Additionally, *blue* MFLs exhibit slipping reconnection in the  $P(P')$  region, thus tracing the region of observed brightening  $b_2$  (see animations). Importantly, the sequence of change  $P_4(P'_4) \rightarrow P(P')$  remains identical across all the simulations.

### 5.4. Transient Magnetic Null

Astoundingly, all the three simulations show generation of a magnetic null point in the near neighborhood of the HFT. In the following we present a detailed analysis of the null-point generation by following two different sets of *green* and *purple* magnetic field lines during their evolution. The evolution for simulations  $S_1$ ,  $S_2$ , and  $S_3$  is depicted in the *left*, *middle*, and *right* columns of Figure 16. With the focus of capturing null-point generation, we note that initially, at  $t = 0$ , there is no identifiable magnetic null point, as shown in Panels (a), (d), and (g). The null appear at  $t = 110$  in  $S_1$  as shown in Panel (b), while in the other two simulations, the null point generates at  $t = 400$  and  $t = 300$ , as depicted in Panels (e) and (h), respectively. The null is detected using the same trilinear method used earlier. Interestingly, the null point is located in close proximity of the HFT (near  $b_2$ ) across all the simulations. Subsequently, all the three nulls corresponding to the three simulations disappear (Panels (c), (f), and (i) of Figure 16), prompting us to name it a transient null.

Interestingly, the MFLs constituting the fan plane of the transient nulls contribute toward the observed brightening  $b_2$ . To capture the associated reconnection process, which occurs in



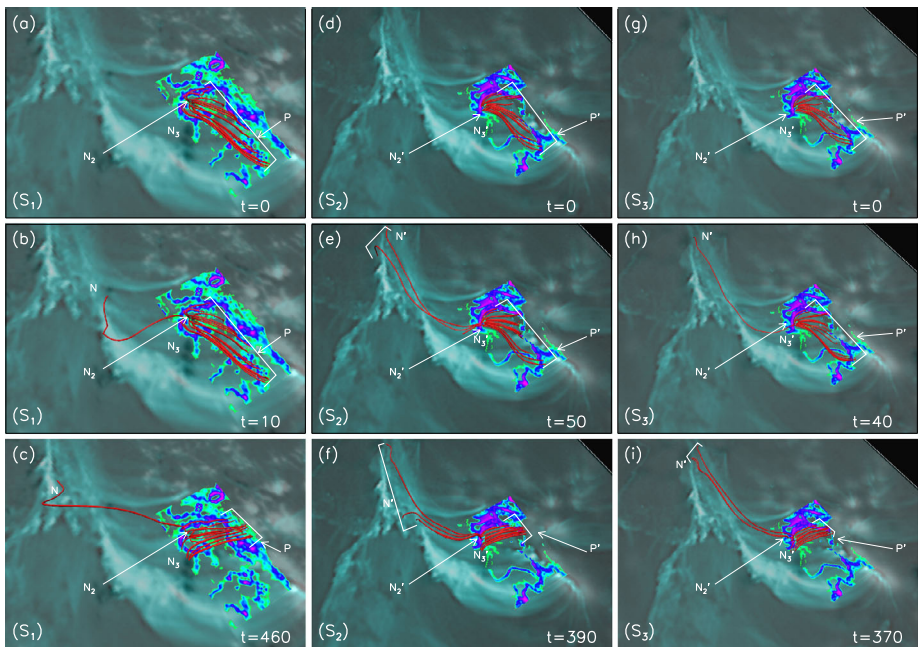


**Figure 14** Snapshots from the simulated evolution of *red* magnetic field lines in the hyperbolic flux tube (HFT) morphology for  $S_1$  (left column),  $S_2$  (middle column), and  $S_3$  (right column). The first row depicts initial field-line configuration, the second row shows the change in footpoint mapping from  $N_2(N_2') \rightarrow N(N')$ , while the third row corresponds to the final morphological arrangement, postadvection. To analyze the associated slipping reconnection, the distribution of  $\ln Q$  is shown at the bottom boundary with the same color coding as in Figure 8. The co-spatiality of observed brightening  $b_2$  with the HFT can be seen from the overlaid line-of-sight magnetogram from SDO/HMI at 02:48 UT along with an image of AR1977 from SDO/AIA in the 131 Å channel at 02:59:56 UT on the bottom boundary (animations available).

a small time window due to the transient property of the null point, we first analyze the field-line configuration slightly before the instance of the null-point appearance (Panels (a), (d), and (g) of Figure 17) for the three simulations. The emphasis here is on the field lines whose footpoints are enclosed by the *red circle*, overlaid on a section of the observed brightening  $b_2$ . During a very small time span, centered at the instance of null-point generation, the footpoints of the fan planes break the flux freezing condition and do not move in the direction of the plasma flow (shown in *black arrows*). The footpoints of the fan plane move in the leftward direction, while the plasma flow vectors are in the rightward direction, as is evident in Panel (b) at  $t = 110$  for  $S_1$ , and in Panels (e) and (h) at  $t = 400$  and  $t = 300$  for the other two simulations. Such slippage of MFLs from the plasma flow are indicative of slipping reconnection (see animations for a clearer view), thus contributing toward the brightening  $b_2$ . Further along the simulated evolution, the null point disappears, as shown in Panels (c), (f), and (i) for the three simulations.

## 6. Summary and Conclusions

The paper explores the influence of the relevant initial conditions on the magnetohydrodynamic simulations of the coronal plasma in the presence of magnetic reconnections. Con-

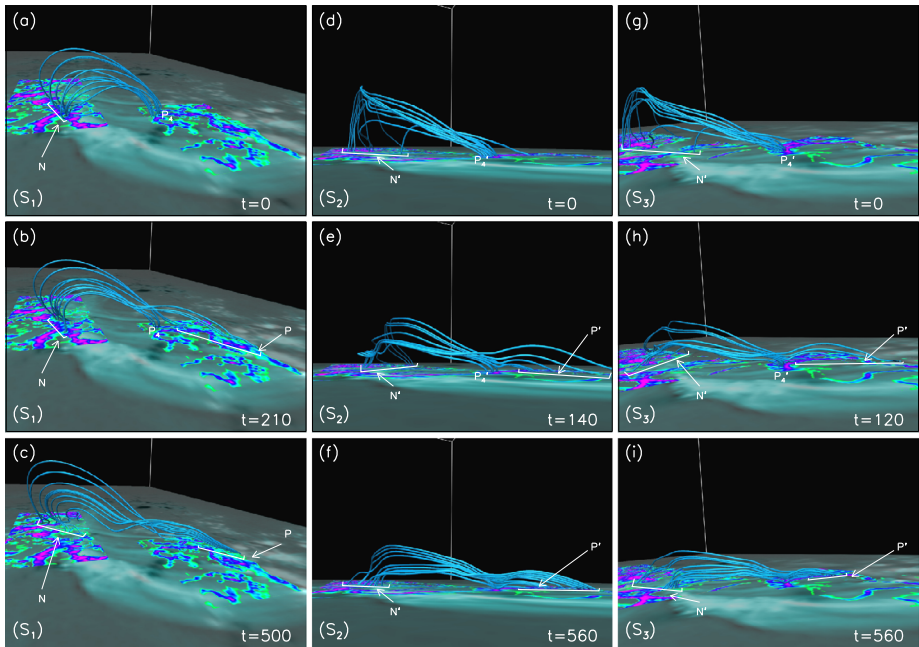


**Figure 15** Snapshots from the simulated evolution of *blue* magnetic field lines in the hyperbolic flux tube (HFT) morphology for  $S_1$  (left column),  $S_2$  (middle column), and  $S_3$  (right column). The *first* row depicts the initial field-line configuration, the *second* row shows the change in footpoint mapping from  $P_4(P'_4) \rightarrow P(P')$  due to slipping reconnection, while the *third* row represents the final morphological structure. To analyze the associated slipping reconnection, the distribution of  $\ln Q$  is shown on the bottom boundary with the same color coding as in Figure 8. The cospatiality of observed brightening  $b_2$  with the HFT can be seen from the overlaid line-of-sight magnetogram from SDO/HMI at 02:48 UT along with an image of AR11977 from SDO/AIA in the 131 Å channel at 02:59:56 UT on the bottom boundary (animations available).

strained by observations, physically relevant initial conditions are generated from nonforce-free and nonlinear force-free extrapolations of AR11977. To ensure the presence of magnetic reconnection, the simulations cover a time span of  $\sim 33$  min, approximately covering the duration of a C6.6 class flare. Comprehensive analysis of the extrapolated magnetic field is presented. The nonlinear force-free field is constructed to have zero Lorentz force, whereas the nonforce-free field is found to exert a small Lorentz force on the coronal plasma. Both fields have nonzero magnetic field and volume current density at coronal heights. The quantitative difference between the extrapolated magnetic fields is investigated by computing the angular deviation ( $\theta$ ) and difference metric ( $d$ ) between the magnetic field vectors. We find that the fraction of computational volume with  $\theta \leq 40^\circ$  and  $d \leq 10$  corresponds to 80% and 99.9%, respectively, which suggests that the two extrapolated magnetic fields are nearly similar. The nonforce-free field shows a slightly better correlation with the measured photospheric field, having Pearson correlation coefficients of 0.99 for the line-of-sight and 0.92 for the transverse magnetic fields, in contrast to 0.96 and 0.88 for the NLFFF extrapolation. Further, morphological analysis reveals the presence of several complex magnetic field line structures around the observed brightenings, having plausible reconnection topologies like magnetic null points, quasiseparatrix layers, and hyperbolic flux tubes in both the extrapolated fields.

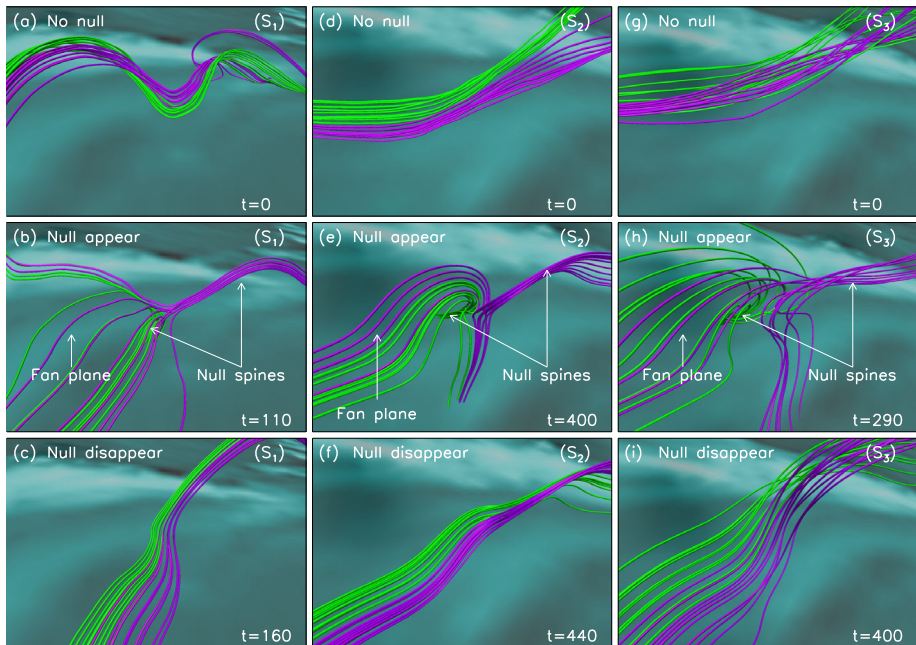


**Figure 16** Snapshots from the simulated evolution of selected *green* and *purple* magnetic field lines to capture the generation of magnetic null in time for  $S_1$  (left column),  $S_2$  (middle column), and  $S_3$  (right column). The *first* row depicts the initial field-line configuration when there is no magnetic null point, the *second* row corresponds to the instance of null-point appearance, while the *last* row captures the disappearance of the null point. The bottom boundary is overlaid with a line-of-sight magnetogram from SDO/HMI at 02:48 UT along with an image of AR11977 from SDO/AIA in the 131 Å channel at 02:59:56 UT (animations available).

To investigate reconnection, MHD evolution initiated with the nonlinear force-free and the nonforce-free extrapolated field has been numerically simulated. The plasma is idealized to have zero physical resistivity, while being viscid, thermodynamically inactive, and incompressible. The simulations are started with three different initial conditions. The NFFF is used to initiate the first simulation ( $S_1$ ), where an implicit Lorentz force drives the plasma dynamics in a self-consistent way. Secondly, we use the NLFFF for simulation ( $S_2$ ) where the residual numerical forces drive the plasma. In the third simulation ( $S_3$ ), an external flow is provided to the initial NLFFF, keeping the strength of the resulting perturbation small. The comparison of simulations for volume-integrated quantities such as free magnetic and total magnetic energy suggests a near independence of the magnetohydrodynamic evolution with respect to the initial conditions in the presence of magnetic reconnection. Further, investigation of changes in magnetic field line connectivity during reconnection at magnetic field line morphologies such as the null point and hyperbolic flux tube (HFT) indicate a near similarity, except for a time delay between events in  $S_1$ ,  $S_2$ , and  $S_3$ . The delay is expected as the initial Lorentz force starting the evolution in the three cases are of different magnitudes. A few of the results are worth summarizing.

The order of dissipated free magnetic energy ( $\sim 10^{31}$  ergs) and percentage decrement in total magnetic energy ( $\sim 5.5\%$ ) are nearly similar across all the simulations. In the magnetic null-point topology (Figure 12), the lower spine ( $S_1$ ) is lost with time owing to reconnection at the null point, irrespective of the initial conditions. Similarly, in the HFT morphology, the sequence of changes in field-line connectivity associated with reconnection is

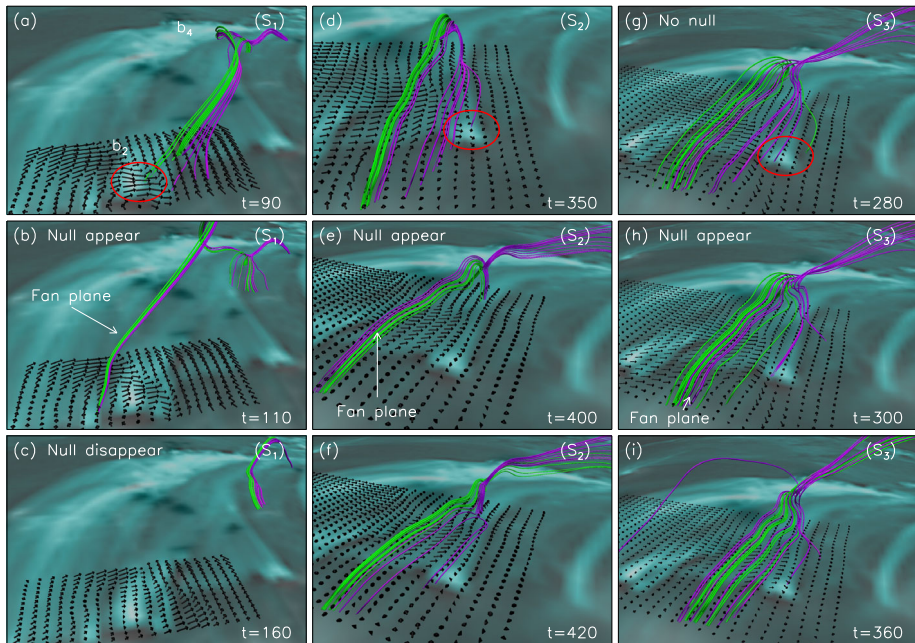


**Figure 17** Snapshots from the simulated evolution of selected *green* and *purple* magnetic field lines to illustrate the contribution of transient magnetic null in the observed brightening  $b_2$ , as shown in Panel (a), for  $S_1$  (left column),  $S_2$  (middle column), and  $S_3$  (right column). The first row shows the initial field-line configuration, just before the instance of null-point generation. The *red circle* indicates the region of interest in terms of observed brightening, while the *black arrows* represent the flow velocity vectors. The *second row* highlights the footpoint movement of the fan plane, which does not follow the direction of plasma flow (*black arrows*). The third row depicts the instance where the null point is lost in time. The bottom boundary is overlaid with a line-of-sight magnetogram from SDO/HMI at 02:48 UT along with an image of AR11977 from SDO/AIA in the 131 Å channel at 02:59:56 UT.

essentially the same, independent of the initial conditions. For *yellow* MFLs (Figure 13), the sequence follows  $N(N') \rightarrow N_3(N'_3) \rightarrow N(N')$ . Similarly, for *red* MFLs (Figure 14), the sequence is  $N_2(N'_2) \rightarrow N(N') \rightarrow$  advection from  $N_2(N'_2)$  to  $N_3(N'_3) \rightarrow N(N')$  and for *blue* MFLs (Figure 15), the sequence is  $P_4(P'_4) \rightarrow P(P')$ . The analysis of multiple sets of field lines belonging to the same HFT morphology suggests that in general, there exist multiple contributions to a particular brightening and it is difficult to isolate the relative importance of various MFL sets. Most importantly, we find spontaneous appearance and disappearance of a magnetic null (referred to as a transient null) near HFT across all the simulations. Such spontaneous generation indicates the possibility that the field-line evolution is independent of the initial conditions. Moreover, the footpoints of the fan plane of this transient null are cospatial with the brightening labeled as  $b_2$  in Figure 2—suggesting that in all three simulations, reconnections associated with this spontaneously generated null contribute to the brightening and hence, has an observable signature. Further, this implies that transient structures produced during the magnetohydrodynamic simulation must be taken into account for a complete analysis of the observed brightenings in solar corona.

The near insensitivity of magnetic field line evolution during reconnection to the particular initial condition inevitably leads to the conclusion that the nonforce-free and force-free extrapolations can both be used as valid initial conditions in data-constrained simulations.

Obviously, this inference is based on a single active-region study using idealized numerical simulations and more such numerical experiments are required to arrive at a statistically significant conclusion that we keep for future explorations.

**Supplementary Information** The online version contains supplementary material available at <https://doi.org/10.1007/s11207-022-02016-2>.

**Data Availability** The data sets generated during and/or analyzed during the current study are available from the corresponding author on reasonable request.

## Declarations

**Disclosure of Potential Conflicts of Interest** The authors declare that they have no conflicts of interest.

## References

- Aly, J.J.: 1989, On the reconstruction of the nonlinear force-free coronal magnetic field from boundary data. *Solar Phys.* **120**, 19. DOI. ADS.
- Amari, T., Canou, A., Aly, J.-J.: 2014, Characterizing and predicting the magnetic environment leading to solar eruptions. *Nature* **514**, 465. DOI. ADS.
- Aschwanden, M.J.: 2005, *Physics of the Solar Corona. An Introduction with Problems and Solutions*, 2nd edn. ADS.
- Bhattacharyya, R., Janaki, M.S.: 2004, Dissipative relaxed states in two-fluid plasma with external drive. *Phys. Plasmas* **11**, 5615. DOI. ADS.
- Bhattacharyya, R., Low, B.C., Smolarkiewicz, P.K.: 2010, On spontaneous formation of current sheets: untwisted magnetic fields. *Phys. Plasmas* **17**, 112901. DOI. ADS.
- Bhattacharyya, R., Janaki, M.S., Dasgupta, B., Zank, G.P.: 2007, Solar arcades as possible minimum dissipative relaxed states. *Solar Phys.* **240**, 63. DOI. ADS.
- Bobra, M.G., Sun, X., Hoeksema, J.T., Turmon, M., Liu, Y., Hayashi, K., Barnes, G., Leka, K.D.: 2014, The helioseismic and magnetic imager (HMI) vector magnetic field pipeline: SHARPs - space-weather HMI active region patches. *Solar Phys.* **289**, 3549. DOI. ADS.
- Calabretta, M.R., Greisen, E.W.: 2002, Representations of celestial coordinates in FITS. *Astron. Astrophys.* **395**, 1077. DOI. ADS.
- Chandrasekhar, S., Kendall, P.C.: 1957, On force-free magnetic fields. *Astrophys. J.* **126**, 457. DOI. ADS.
- Gary, G.A.: 2001, Plasma beta above a solar active region: rethinking the paradigm. *Solar Phys.* **203**, 71. DOI. ADS.
- Ghizaru, M., Charbonneau, P., Smolarkiewicz, P.K.: 2010, Magnetic cycles in global large-eddy simulations of solar convection. *Astrophys. J. Lett.* **715**, L133. DOI. ADS.
- Grinstein, F.F., Margolin, L.G., Rider, W.: 2007, *Implicit Large Eddy Simulation: Computing Turbulent Fluid Dynamics*, Cambridge University Press, Cambridge.
- Haynes, A.L., Parnell, C.E.: 2007, A trilinear method for finding null points in a three-dimensional vector space. *Phys. Plasmas* **14**, 082107. DOI. ADS.
- Hu, Q., Dasgupta, B.: 2008, An improved approach to non-force-free coronal magnetic field extrapolation. *Solar Phys.* **247**, 87. DOI. ADS.
- Inoue, S., Hayashi, K., Kusano, K.: 2016, Structure and stability of magnetic fields in solar active region 12192 based on nonlinear force-free field modeling. *Astrophys. J.* **818**, 168. DOI.
- Inoue, S., Hayashi, K., Magara, T., Choe, G.S., Park, Y.D.: 2014, Magnetohydrodynamic simulation of the X2.2 solar flare on 2011 February 15. I. Comparison with the observations. *Astrophys. J.* **788**, 182. DOI. ADS.
- Inoue, S., Hayashi, K., Magara, T., Choe, G.S., Park, Y.D.: 2015, Magnetohydrodynamic simulation of the X2.2 solar flare on 2011 February 15. II. Dynamics connecting the solar flare and the coronal mass ejection. *Astrophys. J.* **803**, 73. DOI. ADS.
- Jiang, C., Feng, X., Wu, S.T., Hu, Q.: 2013, Magnetohydrodynamic simulation of a sigmoid eruption of active region 11283. *Astrophys. J. Lett.* **771**, L30. DOI. ADS.
- Jiang, C., Wu, S.T., Feng, X., Hu, Q.: 2016, Data-driven magnetohydrodynamic modelling of a flux-emerging active region leading to solar eruption. *Nat. Commun.* **7**, 11522. DOI. ADS.
- Joshi, N.C., Joshi, B., Mitra, P.K.: 2021, Evolutionary stages and triggering process of a complex eruptive flare with circular and parallel ribbons. *Mon. Not. Roy. Astron. Soc.* **501**, 4703. DOI. ADS.

- Khlystova, A., Toriumi, S.: 2017, Photospheric velocity structures during the emergence of small active regions on the sun. *Astrophys. J.* **839**, 63. DOI. ADS.
- Kliem, B., Török, T.: 2006, Torus instability. *Phys. Rev. Lett.* **96**, 255002. DOI. ADS.
- Kliem, B., Linton, M.G., Török, T., Karlický, M.: 2010, Reconnection of a kinking flux rope triggering the ejection of a microwave and hard X-ray source II. Numerical modeling. *Solar Phys.* **266**, 91. DOI. ADS.
- Kliem, B., Su, Y.N., van Ballegoijen, A.A., DeLuca, E.E.: 2013, Magnetohydrodynamic modeling of the solar eruption on 2010 April 8. *Astrophys. J.* **779**, 129. DOI. ADS.
- Kumar, S., Bhattacharyya, R.: 2016, Continuous development of current sheets near and away from magnetic nulls. *Phys. Plasmas* **23**, 044501. DOI. ADS.
- Kumar, S., Bhattacharyya, R., Joshi, B., Smolarkiewicz, P.K.: 2016, On the role of repetitive magnetic reconnections in evolution of magnetic flux ropes in solar corona. *Astrophys. J.* **830**, 80. DOI. ADS.
- Kumar, S., Nayak, S.S., Prasad, A., Bhattacharyya, R.: 2021, Magnetic reconnections in the presence of three-dimensional magnetic nulls and quasi-separatrix layers. *Solar Phys.* **296**, 26. DOI. ADS.
- Lemen, J.R., Title, A.M., Akin, D.J., Boerner, P.F., Chou, C., Drake, J.F., Duncan, D.W., Edwards, C.G., Friedlaender, F.M., Heyman, G.F., Hurlburt, N.E., Katz, N.L., Kushner, G.D., Levay, M., Lindgren, R.W., Mathur, D.P., McFeaters, E.L., Mitchell, S., Rehse, R.A., Schrijver, C.J., Springer, L.A., Stern, R.A., Tarbell, T.D., Wuelsel, J.-P., Wolfson, C.J., Yanari, C., Bookbinder, J.A., Cheimets, P.N., Caldwell, D., Deluca, E.E., Gates, R., Golub, L., Park, S., Podgorski, W.A., Bush, R.I., Scherrer, P.H., Gummis, M.A., Smith, P., Auker, G., Jerram, P., Pool, P., Soufii, R., Windt, D.L., Beardsley, S., Clapp, M., Lang, J., Waltham, N.: 2012, The atmospheric imaging assembly (AIA) on the solar dynamics observatory (SDO). *Solar Phys.* **275**, 17. DOI. ADS.
- Liu, R., Kliem, B., Titov, V.S., Chen, J., Wang, Y., Wang, H., Liu, C., Xu, Y., Wiegmann, T.: 2016, Structure, stability, and evolution of magnetic flux ropes from the perspective of magnetic twist. *Astrophys. J.* **818**, 148. DOI.
- Mahajan, S.M., Yoshida, Z.: 1998, Double curl Beltrami flow: diamagnetic structures. *Phys. Rev. Lett.* **81**, 4863. DOI. ADS.
- Margolin, L.G., Rider, W.J., Grinstein, F.F.: 2006, Modeling turbulent flow with implicit LES. *J. Turbul.* **7**, N15. DOI.
- Mitra, P.K., Joshi, B., Prasad, A., Veronig, A.M., Bhattacharyya, R.: 2018, Successive flux rope eruptions from  $\delta$ -sunspots region of NOAA 12673 and associated X-class eruptive flares on 2017 September 6. *Astrophys. J.* **869**, 69. DOI. ADS.
- Mitra, P.K., Joshi, B., Veronig, A.M., Chandra, R., Dissauer, K., Wiegmann, T.: 2020, Eruptive-impulsive homologous M-class flares associated with double-decker flux rope configuration in minisigmoid of NOAA 12673. *Astrophys. J.* **900**, 23. DOI. ADS.
- Nakagawa, Y., Raadu, M.A.: 1972, On practical representation of magnetic field. *Solar Phys.* **25**, 127. DOI. ADS.
- Nayak, S.S., Bhattacharyya, R., Kumar, S.: 2021, Magnetohydrodynamics model of an X-class flare in NOAA active region 12017 initiated with non-force-free extrapolation. *Phys. Plasmas* **28**, 024502. DOI. ADS.
- Nayak, S.S., Bhattacharyya, R., Prasad, A., Hu, Q., Kumar, S., Joshi, B.: 2019, A data-constrained magnetohydrodynamic simulation of successive events of blowout jet and C-class flare in NOAA AR 12615. *Astrophys. J.* **875**, 10. DOI. ADS.
- Pariat, É.: 2020, In: MacTaggart, D., Hillier, A. (eds.) *Using Magnetic Helicity, Topology, and Geometry to Investigate Complex Magnetic Fields*, Springer, Cham, 145. ISBN 978-3-030-16343-3. DOI.
- Pesnell, W.D., Thompson, B.J., Chamberlin, P.C.: 2012, The solar dynamics observatory (SDO). *Solar Phys.* **275**, 3. DOI. ADS.
- Prasad, A., Bhattacharyya, R., Hu, Q., Kumar, S., Nayak, S.S.: 2018, A magnetohydrodynamic simulation of magnetic null-point reconnections in NOAA AR 12192, initiated with an extrapolated non-force-free field. *Astrophys. J.* **860**, 96. DOI. ADS.
- Prusa, J.M., Smolarkiewicz, P.K., Wyszogrodzki, A.A.: 2008, EULAG, a computational model for multiscale flows. *Comput. Fluids* **37**, 1193. DOI.
- Rempel, M., Cheung, M., Chintzoglou, G.: 2021, Flare simulations with the MURaM radiative MHD code. In: *43rd COSPAR Scientific Assembly. Held 28 January - 4 February* **43**, 1772. ADS.
- Scherrer, P.H., Schou, J., Bush, R.I., Kosovichev, A.G., Bogart, R.S., Hoeksema, J.T., Liu, Y., Duvall, T.L., Zhao, J., Title, A.M., Schrijver, C.J., Tarbell, T.D., Tomczyk, S.: 2012, The helioseismic and magnetic imager (HMI) investigation for the solar dynamics observatory (SDO). *Solar Phys.* **275**, 207. DOI. ADS.
- Schou, J., Scherrer, P.H., Bush, R.I., Wachter, R., Couvidat, S., Rabello-Soares, M.C., Bogart, R.S., Hoeksema, J.T., Liu, Y., Duvall, T.L., Akin, D.J., Allard, B.A., Miles, J.W., Rairden, R., Shine, R.A., Tarbell, T.D., Title, A.M., Wolfson, C.J., Elmore, D.F., Norton, A.A., Tomczyk, S.: 2012, Design and ground calibration of the helioseismic and magnetic imager (HMI) instrument on the solar dynamics observatory (SDO). *Solar Phys.* **275**, 229. DOI. ADS.

- Shibata, K., Magara, T.: 2011, Solar flares: magnetohydrodynamic processes. *Living Rev. Solar Phys.* **8**, 6. DOI. ADS.
- Smolarkiewicz, P.K.: 2006, Multidimensional positive definite advection transport algorithm: an overview. *Int. J. Numer. Methods Fluids* **50**, 1123. DOI. ADS.
- Smolarkiewicz, P.K., Charbonneau, P.: 2013, EULAG, a computational model for multiscale flows: an MHD extension. *J. Comput. Phys.* **236**, 608. DOI. ADS.
- Titov, V.S., Démoulin, P.: 1999, Basic topology of twisted magnetic configurations in solar flares. *Astron. Astrophys.* **351**, 707. ADS.
- Titov, V.S., Hornig, G., Démoulin, P.: 2002, Theory of magnetic connectivity in the solar corona. *J. Geophys. Res.* **107**, 1164. DOI. ADS.
- Vekstein, G.: 2016, Storing free magnetic energy in the solar corona. *J. Plasma Phys.* **82**, 925820401. DOI. ADS.
- Warren, H.P., Crump, N.A., Ugarte-Urra, I., Sun, X., Aschwanden, M.J., Wiegelmann, T.: 2018, Toward a quantitative comparison of magnetic field extrapolations and observed coronal loops. *Astrophys. J.* **860**, 46. DOI. ADS.
- Wheatland, M.S., Sturrock, P.A., Roumeliotis, G.: 2000, An optimization approach to reconstructing force-free fields. *Astrophys. J.* **540**, 1150. DOI. ADS.
- Wiegelmann, T.: 2004, Optimization code with weighting function for the reconstruction of coronal magnetic fields. *Solar Phys.* **219**, 87. DOI. ADS.
- Wiegelmann, T., Inhester, B.: 2010, How to deal with measurement errors and lacking data in nonlinear force-free coronal magnetic field modelling? *Astron. Astrophys.* **516**, A107. DOI. ADS.
- Wiegelmann, T., Inhester, B., Sakurai, T.: 2006, Preprocessing of vector magnetograph data for a nonlinear force-free magnetic field reconstruction. *Solar Phys.* **233**, 215. DOI. ADS.
- Wiegelmann, T., Sakurai, T.: 2021, Solar force-free magnetic fields. *Living Rev. Solar Phys.* **18**, 1. DOI. ADS.
- Wiegelmann, T., Thalmann, J.K., Inhester, B., Tadesse, T., Sun, X., Hoeksema, J.T.: 2012, How should one optimize nonlinear force-free coronal magnetic field extrapolations from SDO/HMI vector magnetograms? *Solar Phys.* **281**, 37. DOI. ADS.
- Yoshida, Z., Giga, Y.: 1990, Remarks on spectra of operator rot. *Math. Z.* **204**, 235. DOI.
- Zhao, J., Li, H., Pariat, E., Schmieder, B., Guo, Y., Wiegelmann, T.: 2014, Temporal evolution of the magnetic topology of the NOAA active region 11158. *Astrophys. J.* **787**, 88. DOI. ADS.
- Zweibel, E.G., Yamada, M.: 2016, Perspectives on magnetic reconnection. *Proc. Roy. Soc. London Ser. A* **472**, 20160479. DOI. ADS.